



# Reactivity and stability investigation of supported molybdenum oxide catalysts for the hydrodeoxygenation (HDO) of m-cresol



Manish Shetty<sup>1</sup>, Karthick Murugappan<sup>1</sup>, Teerawit Prasomsri, William H. Green, Yuriy Román-Leshkov<sup>\*</sup>

Department of Chemical Engineering, Massachusetts Institute of Technology, Cambridge, MA 02139, United States

## ARTICLE INFO

### Article history:

Received 19 May 2015

Revised 25 July 2015

Accepted 31 July 2015

Available online 15 September 2015

This article is dedicated to Prof. Jean-Pierre Gilson on the occasion of his birthday. His seminal work in the areas of adsorption, catalysis, zeolite chemistry, and biomass conversion inspired us to undertake the present line of research involving reducible metal oxides for the deoxygenation of biomass-derived molecules. We wholeheartedly congratulate Jean-Pierre, wishing him continuing success in his work.

### Keywords:

Hydrodeoxygenation (HDO)  
Lignin-derived oxygenates  
m-Cresol  
Supported molybdenum oxides  
Metal-support interaction  
Biomass conversion

## ABSTRACT

The vapor-phase hydrodeoxygenation (HDO) of m-cresol is investigated at 593 K and H<sub>2</sub> pressures ≤ 1 bar for supported catalysts comprised of 10 wt% MoO<sub>3</sub> dispersed over SiO<sub>2</sub>, γ-Al<sub>2</sub>O<sub>3</sub>, TiO<sub>2</sub>, ZrO<sub>2</sub>, and CeO<sub>2</sub>. Reactivity data show that all catalysts selectively cleave C–O bonds without saturating the aromatic ring, thus effectively transforming m-cresol into toluene at moderate to high conversions. MoO<sub>3</sub>/ZrO<sub>2</sub> and MoO<sub>3</sub>/TiO<sub>2</sub> feature the highest initial site time yields (23.4 and 13.9 h<sup>-1</sup>, respectively) and lowest first-order deactivation rate constants (0.013 and 0.006 h<sup>-1</sup>, respectively) of all catalysts tested after ca. 100 h on stream. Characterization studies demonstrate that the supports play an important role in stabilizing partially reduced, coordinatively unsaturated (CU) sites in surface oligomeric Mo moieties. Post-reaction X-ray photoelectron spectroscopy shows that the catalysts with higher activity feature larger proportions of intermediate oxidation species (Mo<sup>5+</sup> and Mo<sup>3+</sup>). In contrast, the catalysts with lower reactivity show different oxidation states: bulk MoO<sub>3</sub> features mostly Mo<sup>4+</sup> and metallic Mo species, while MoO<sub>3</sub>/CeO<sub>2</sub> features a high proportion of Mo<sup>6+</sup> species. An inverse correlation is established between the catalyst activity and both the maximum hydrogen consumption temperature obtained during temperature programmed reduction, and the support cation electronegativity (with the exception of MoO<sub>3</sub>/CeO<sub>2</sub>).

© 2015 Elsevier Inc. All rights reserved.

## 1. Introduction

Catalytic fast pyrolysis (CFP) is an attractive technology to convert biomass into fuel additives and value-added chemicals [1–4]. Zeolites have recently been shown to be highly effective catalysts for converting lignocellulosic biomass to gasoline-range aromatics via CFP [5–7]. However, given that lignocellulosic biomass is inherently hydrogen poor with a H/C<sub>eff</sub> ratio (defined as [(H – 2O)/C]) ranging from 0 to 0.3, the maximum yield of hydrocarbons that can be obtained by upgrading it in the absence of external H<sub>2</sub> is severely limited by stoichiometry. As such, upgrading with zeolites typically results in aromatic and olefinic hydrocarbon yields near 30% concomitant with high coke formation [5,8]. Conventional hydrotreating catalysts (e.g., sulfided CoMo and NiMo) and supported noble metal catalysts have been reported to produce stable and energy dense products from pyrolysis oils [2,9–12]. However,

they require high H<sub>2</sub> pressures that lead to aromatic ring hydrogenation, resulting in reduced octane number and increased H<sub>2</sub> consumption [2]. In light of these challenges, it is desirable to develop technologies that use H<sub>2</sub> to selectively cleave C–O bonds without aromatic ring saturation, at preferably low H<sub>2</sub> pressures.

Recently, Román-Leshkov and coworkers demonstrated that several reducible metal oxides, including MoO<sub>3</sub>, are effective hydrodeoxygenation (HDO) catalysts capable of selectively cleaving C–O bonds in various bio-derived oxygenates to produce olefinic and aromatic hydrocarbons. Remarkably, the HDO reactions were catalyzed at mild conditions of 593 K and H<sub>2</sub> partial pressures ≤ 1 bar [13,14]. It was hypothesized that HDO occurs via an oxygen vacancy driven mechanism over a partially carburized molybdenum surface. The characterization data showed that Mo<sup>5+</sup> species were important for maintaining HDO activity, and suggested that the phase transformation of MoO<sub>3</sub> to an oxycarbohydride (MoO<sub>x</sub>C<sub>y</sub>H<sub>z</sub>) played a critical role in stabilizing these Mo<sup>5+</sup> species by preventing the over-reduction to less active Mo<sup>4+</sup> species [14–16].

<sup>\*</sup> Corresponding author.

E-mail address: [yroman@mit.edu](mailto:yroman@mit.edu) (Y. Román-Leshkov).

<sup>1</sup> These authors contributed equally.

High surface area supports are ubiquitously used to increase the dispersion of active Mo species [17–19]. Importantly, some supports have been shown to drastically influence the catalytic activity of Mo species by stabilizing specific oxidation states [20], or by influencing the geometric configurations [21], electronic properties [22], and prevalence of “high-energy” sites [23]. For instance, the nature of the Mo–O–support bond in surface MoO<sub>x</sub> domains was shown to influence catalytic activity during the oxidative dehydrogenation of alkanes, as well as other oxidation reactions [24–28]. Notably, the increase in the steady-state turn-over frequency (TOF) was observed to inversely correlate with the support cation electronegativity [24,27]. Recently, ZrO<sub>2</sub>, CeO<sub>2</sub>, and TiO<sub>2</sub> have been studied as supports for the HDO of lignin-derived model compounds using CoMoS, MoS<sub>2</sub>, Ni, and Cu–Ni-based catalysts [12,29–31]. To date, however, no comprehensive studies have been performed on supported MoO<sub>3</sub> catalysts for HDO.

In this work, we investigate the influence of supports, including SiO<sub>2</sub>, γ-Al<sub>2</sub>O<sub>3</sub>, TiO<sub>2</sub>, ZrO<sub>2</sub>, and CeO<sub>2</sub>, on the reactivity and stability of dispersed MoO<sub>3</sub> during the hydrodeoxygenation of m-cresol—a model bio-oil compound. Supported catalysts are synthesized with ca. 10 wt% MoO<sub>3</sub> loading, which corresponds to near-monolayer oligomeric MoO<sub>x</sub> species on the support surface. Reactivity studies are performed to identify differences in activity that arise from specific Mo-support interactions. Oxygen chemisorption is used to determine the number of redox-active Mo sites, and initial site time yields (STYs) are then used to compare the performance of different catalysts. Reactivity data are then combined with detailed characterization techniques to identify the genesis of the observed reactivity differences. Post-reaction analysis with X-ray photoelectron spectroscopy (XPS) and temperature programmed oxidation-mass spectrometry (TPO-MS) provide insights on the preferential stabilization of specific Mo oxidation states by each support, as well as overall propensity for coking. These data are then correlated to long-term stability and regenerability properties of the catalyst.

## 2. Experimental

### 2.1. Catalyst materials and synthesis

The feed, m-cresol (99%, Sigma–Aldrich), was used without further purification. H<sub>2</sub> (99.999%), He (99.999%), O<sub>2</sub> (99.999%) and air (dry grade, Airgas) were purchased from Airgas. Molybdenum (VI) oxide (MoO<sub>3</sub>, ≥99.5 wt%), molybdenum (IV) oxide (MoO<sub>2</sub>, ≥99 wt%), and molybdenum carbide (Mo<sub>2</sub>C, ≥99 wt%) were purchased from Sigma–Aldrich. α-Aluminum oxide, α-Al<sub>2</sub>O<sub>3</sub> (100–200 mesh, ≥99 wt%, Sigma–Aldrich) was used as an inert diluent for all reactions. Titanium (IV) oxide, TiO<sub>2</sub> (majority anatase, 21 nm, ≥99.5 wt%), and silicon oxide, SiO<sub>2</sub> (5–15 nm, 99.5 wt%) were purchased from Sigma–Aldrich and used directly as supports. γ-Aluminum oxide (γ-Al<sub>2</sub>O<sub>3</sub>, 0.3175 cm pellets, Alfa Aesar) was ground and sieved with a 200 mesh (<74 μm) for use as support. Zirconium (IV) oxide (ZrO<sub>2</sub>) and cerium (IV) oxide (CeO<sub>2</sub>) nanoparticles were synthesized using previously reported methods [32].

Supported 10 wt% MoO<sub>3</sub> catalysts were prepared using wet impregnation method. For a batch of 5 g of supported catalyst, 5 ml aqueous solution of 0.614 g ammonium paramolybdate tetra (para) hydrate ((NH<sub>4</sub>)<sub>6</sub>Mo<sub>7</sub>O<sub>24</sub>·4H<sub>2</sub>O, 99%, Alfa Aesar) was added dropwise to the support (4.5 g) under vigorous stirring. The sample was then dried at 373 K for 12 h and calcined at 823 K (ramp rate 10 K min<sup>-1</sup>) in air at a flow rate of 100 ml min<sup>-1</sup> for 3 h. Bulk MoO<sub>3</sub> was activated under identical conditions.

### 2.2. Catalyst activity measurement and product analysis

Catalytic activity and stability experiments were carried out in a vapor-phase packed-bed down-flow reactor. The reactor consisted

of a stainless-steel tube (0.95 cm OD) with wall thickness (0.089 cm) mounted in a single-zone furnace (Applied Test Systems, Series 3210, 850W/115V). The temperature was controlled by a temperature controller (Digi-Sense, model 68900-10) connected to a K-type thermocouple (Omega, model TJ36-CAXL-116u) mounted downstream in direct contact with the catalyst bed. The catalyst was mixed with α-Al<sub>2</sub>O<sub>3</sub> (total 1 g) and packed between two inert layers of α-Al<sub>2</sub>O<sub>3</sub> (1.5 g each) and kept in the middle of the furnace. The total volume of the bed was approximately 2 cm<sup>3</sup>. Prior to reaction, the reactor temperature was ramped at a rate of 6 K min<sup>-1</sup> under He to the reaction temperature of 593 K. Next, m-cresol was delivered into the reactor via a capillary tube connected to a syringe pump (Harvard Apparatus, model 703005) and mixed with H<sub>2</sub> gas at the inlet of the reactor. Flow rates were adjusted to obtain weight hourly space velocity (WHSV) values of 8.27 h<sup>-1</sup>.

$$\text{WHSV (h}^{-1}\text{)} = \frac{\text{mass flow rate of reactant fed}}{\text{mass of equivalent MoO}_3 \text{ loaded}} \quad (1)$$

The reactor effluent lines were heated to 523 K to prevent any condensation of effluents. The effluents were analyzed and quantified via an online gas chromatographer (GC) equipped with a mass selective detector for identification (MSD, Agilent Technologies, model 5975 C) and a flame ionization detector for quantification (FID, Agilent Technologies, model 7890 A). The GC was fitted with a DB-5 column (Agilent, 30 m × 0.25 mm ID × 0.25 μm). The GC parameters used for analysis are as follows: detector temperature 573 K, injector temperature 548 K, split ratio 1:20. The initial and final oven temperatures were 343, and 473 K, with a ramp of 8 K min<sup>-1</sup>.

The following definitions were used to quantify experimental data:

$$\text{Conversion (\%)} = \frac{\text{moles of carbon of reactant consumed}}{\text{moles of carbon of reactant fed}} \times 100 \quad (2)$$

$$\begin{aligned} \text{Rate of conversion (mmol h}^{-1} \text{ g}_{\text{MoO}_3}^{-1}\text{)} \\ = \frac{\text{molar flow rate of reactant consumed}}{\text{mass of equivalent MoO}_3 \text{ loaded}} \end{aligned} \quad (3)$$

$$\begin{aligned} \text{Selectivity to hydrocarbons (\%)} \\ = \frac{\text{moles of carbon of hydrocarbons in product}}{\text{moles of carbon of reactant consumed}} \times 100 \end{aligned} \quad (4)$$

$$\text{Yield (\%)} = \frac{\text{moles of carbon of product}}{\text{moles of carbon of reactant fed}} \times 100 \quad (5)$$

The reaction was run in the absence of external and internal mass-transfer limitations (Supporting Information). For most catalysts, initial reactivity data were obtained by operating at low conversions (<14%). The initial rates for MoO<sub>3</sub>/TiO<sub>2</sub> and MoO<sub>3</sub>/ZrO<sub>2</sub> were estimated from high-conversion data, after establishing a zero-order dependence with respect to the oxygenate concentration (Fig. S1, Supporting Information). The catalyst deactivation rate constants were obtained by fitting deactivation profiles to a first-order deactivation model, as reported previously [13,14,33].

### 2.3. Catalyst characterization

All pre-reaction catalyst characterizations were carried out on calcined samples. Powder X-ray diffraction (PXRD) patterns were collected using a Bruker D8 diffractometer with Nickel-filtered Cu Kα radiation (λ = 1.5418 Å). Diffraction data were recorded on a 2D image plate rotated at a speed of 15 rpm, between 2θ values of 20–90° and a total scan time of 30 min. The diffraction patterns

were normalized to maximum peak intensity for each catalyst. Raman spectroscopy was performed on a HORIBA Jobin Yvon using 532 nm laser with a maximum power of 100 mW, and at an optical magnification of 50 $\times$ . The spectra were collected from Raman shifts between 200 and 1200  $\text{cm}^{-1}$  and were normalized to the maximum peak intensity for each catalyst. The spectra between 750 and 1050  $\text{cm}^{-1}$  were similarly normalized to study the dispersion of Mo species on the surface of the support. Diffuse reflectance UV–Vis spectra were recorded on a Cary 5000 (Varian) instrument equipped with a Praying Mantis diffuse reflectance accessory (Harriick Scientific Products) using  $\text{BaSO}_4$  (Sigma–Aldrich, 99%) as a white reference. Reflectance was converted to absorbance using the Kubelka–Munk function  $[F(R_\infty)]$ . The absorption-edge energy was calculated using the  $x$ -intercept of the straight line fitted through low energy rise of spectra,  $[F(R_\infty)hv]^2$  plotted as a function of  $hv$ , where  $hv$  is the energy of an incident photon, as previously reported [34].

Surface area measurements and oxygen chemisorption experiments were carried out on Quantachrome Autosorb iQ automated gas sorption system. The surface area was determined using nitrogen adsorption–desorption experiments at a liquid nitrogen temperature (77 K) using the Brunauer–Emmett–Teller (BET) theory [35]. Oxygen chemisorption was carried out on catalyst samples at 623 K. The samples were treated under He at 393 K for 0.5 h, before being pre-reduced in a flow of  $\text{H}_2$  for 2 h at 623 K. The chemisorption cell was then evacuated for 2 h prior to oxygen adsorption. Weakly adsorbed  $\text{O}_2$  was removed after first adsorption by degassing, and the adsorption isotherm was collected again. The difference between the first and second isotherms was plotted and extrapolated to zero pressure to determine the amount of irreversibly adsorbed  $\text{O}_2$ . The oxygen chemisorption data were used to quantify redox-active Mo species using Eq. (6). The oxygen uptake from the bare support was subtracted from the oxygen uptake of the supported catalyst to determine the uptake from the Mo species. The areal rate of conversion and site time yield (STY) were calculated from the BET surface area and measured redox-active Mo species, respectively, as follows:

Moles of redox active Mo species

$$= 2 \times \text{oxygen uptake in mol g}^{-1} \times \text{catalyst mass in g} \quad (6)$$

$$\text{Redox active Mo species (\%)} = \frac{2 \times \text{oxygen uptake in mol g}^{-1}}{\text{Mo loading in mol g}^{-1}} \times 100 \quad (7)$$

Areal rate of conversion ( $\mu\text{mol h}^{-1} \text{m}^{-2}$ )

$$= \frac{\text{Rate of conversion}}{\text{BET surface area of catalyst}} \quad (8)$$

$$\text{Site time yield (h}^{-1}\text{)} = \frac{\text{molar flow rate of HDO product (toluene) formed}}{\text{moles of redox active Mo species}} \quad (9)$$

Temperature programmed reduction (TPR) was performed in a quartz U-tube setup connected to a mass spectrometer (MS, Hiden Analytical HPR-20/QIC). A quartz U-tube was loaded with a bed of either supported catalyst (400 mg), or support (360 mg). The catalyst bed was in contact with a K-type thermocouple (Omega, model TJ36-CAXL-116u), which was connected to a temperature controller (Digi-Sense, model 68900-10). The U-tube was placed in a furnace (Carbolite<sup>®</sup>, model GTF 11/50/750B, 575W/115 V) connected to the temperature controller. Samples were calcined in  $\text{O}_2$  (100  $\text{ml min}^{-1}$ ) at 773 K for 2 h (ramp rate 8.3  $\text{K min}^{-1}$ ) and cooled under Ar (high purity, Airgas) to room temperature. The temperature was then increased to 873 K at a ramp rate of

2  $\text{K min}^{-1}$  under a gas mixture of 1%  $\text{H}_2$ , 1% Ar, and balance He, at a total flow rate of 50  $\text{ml min}^{-1}$ . The evolution of  $\text{H}_2\text{O}$  ( $m/z = 18$ ), consumption of  $\text{H}_2$  ( $m/z = 2$ ), and the Ar ( $m/z = 40$ ) signal were tracked using MS, where Ar was used as an internal standard. The temperature corresponding to the peak consumption of  $\text{H}_2$  is referred to as the temperature of maximum consumption ( $T_{\text{max}}$ ).

The nature and quantity of deposited carbon species on post-reaction catalysts were analyzed by TPO-MS, using a thermogravimetric analyzer (TGA, TA Instruments TGA-Q500) combined with a mass spectrometer (MS, Hiden Analytical HPR-20/QIC). A gas mixture of 1%  $\text{O}_2$ , 1% Ar, and balance He (Airgas) was used at a total flow rate of 20  $\text{ml min}^{-1}$ . The temperature was equilibrated at 303 K and ramped at 7.5  $\text{K min}^{-1}$  to 923 K. The  $\text{CO}_2$  ( $m/z = 44$ ) and Ar ( $m/z = 40$ ) signals (internal standard) were monitored using the MS. The amount of carbonaceous species was quantified by calculating the evolved  $\text{CO}_2$  against a calibration curve prepared using a graphite standard (powder, <20  $\mu\text{m}$ , synthetic, Sigma–Aldrich).

XPS was performed using a PHI Versaprobe II instrument equipped with a multi-channel hemispherical analyzer and an aluminum anode X-ray source operating at 100 W, featuring a 100  $\mu\text{m}$  beam scanned over a 1.4 mm line across the sample surface. A dual-beam charge neutralization system was used with an electron neutralizer bias of 1.2 eV and an Ar ion beam energy of 10 eV. Except for long TOS runs ( $\sim 100$  h), all post-reaction catalyst samples used for XPS analysis were prepared under identical conditions to those used for reactivity measurement, but were not mixed with the  $\alpha\text{-Al}_2\text{O}_3$  diluent to allow for easy recovery. Samples were passivated in a stream of 1%  $\text{O}_2$ , balance  $\text{N}_2$  (Airgas) gas mixture at a flow rate of 100  $\text{ml min}^{-1}$ , and a temperature below 303 K for 1 h after reaction. The catalysts were recovered and immediately moved to glove box for storage in Ar atmosphere prior to analysis. These post-reaction samples were mixed with niobium oxide ( $\text{Nb}_2\text{O}_5$ , 99.99%, Sigma Aldrich) as an internal standard for charge correction. The binding energies were corrected to 207.4 eV ( $\text{Nb } 3d_{5/2}$ ). In the case of long TOS runs, binding energies were corrected to 284.8 eV (C 1s), 182.3 eV ( $\text{Zr } 3d_{5/2}$ ), 458.5 eV ( $\text{Ti } 2p_{3/2}$ ) for bulk  $\text{MoO}_3$ ,  $\text{MoO}_3/\text{ZrO}_2$ , and  $\text{MoO}_3/\text{TiO}_2$  respectively, as the addition of  $\text{Nb}_2\text{O}_5$  would have led to a low signal-to-noise ratio. A 7-point Shirley background correction was then applied to the Mo 3d XPS spectra after charge correction. The composition of Mo oxidation states was estimated by the deconvolution of Mo 3d spectra. The following constraints were used for deconvolution: (1) Splitting energy of 3.15 eV for Mo  $3d_{5/2}$ –Mo  $3d_{3/2}$ , (2) Area intensity ratio of 3:2 for Mo  $3d_{5/2}$ –Mo  $3d_{3/2}$ , and (3) Equal full width at half maximum (FWHM) of Mo  $3d_{5/2}$  and Mo  $3d_{3/2}$ .

Mo loading on the support was determined from elemental analysis using an inductively coupled plasma atomic emission spectrometer (ICP-AES) (Activa-S, HORIBA Scientific). Samples were dissolved in a 1:1 mixture of 48% hydrogen fluoride, (HF, Sigma–Aldrich) and reagent grade nitric acid ( $\text{HNO}_3$ , Sigma–Aldrich). The solution was then redispersed in 2%  $\text{HNO}_3$  before analysis. A 4-point calibration curve was built using dilutions of a 1000 ppm Mo standard. The Mo spectral line at 202.03 nm was used for the ICP-AES analysis.

### 3. Results

#### 3.1. Pre-reaction catalyst characterization

ICP-AES analysis confirmed the  $\text{MoO}_3$  loading on the supported catalysts to be within 1% of the theoretical loading of 10 wt%. Powder X-ray diffraction (PXRD) patterns for the bare supports and the supported catalysts are shown in Fig. 1 and Fig. S2 (Supporting Information). With the exception of  $\text{MoO}_3/\text{TiO}_2$ , no differences

were observed between each set of diffractograms, indicating that there was no change in the topology of support after dispersion of the Mo species. MoO<sub>3</sub>/TiO<sub>2</sub> shows the presence of MoO<sub>3</sub> peaks at  $2\theta = 23.7^\circ$ , and  $34.2^\circ$ , indicating the formation of crystalline MoO<sub>3</sub> clusters. In general, these data suggest that MoO<sub>3</sub> is well dispersed on the support surface. However, we cannot rule out the presence of clusters smaller than the PXRD crystallite size limits of  $\sim 4$  nm. Raman spectroscopy was used to detect any local changes within dispersed molybdenum oxide domains by probing Mo–O vibrational modes of all supported catalysts (Fig. 2 (a) and (b)). Specifically, the  $\bar{\nu}_{\text{antisymmetric}}$  (Mo–O–Mo) and terminal  $\bar{\nu}$  (Mo=O) stretching modes provide information on the local structure of dispersed MoO<sub>x</sub> domains. In agreement with the PXRD results, of all catalysts tested, only MoO<sub>3</sub>/TiO<sub>2</sub> shows bands at 820, and 995 cm<sup>-1</sup> corresponding to crystalline MoO<sub>3</sub>. However, these band intensities are lower than those seen for  $\bar{\nu}$  (Mo=O) at ca. 980 cm<sup>-1</sup>, which correspond to oligomeric octahedral Mo species [36]. Crystalline MoO<sub>3</sub> bands are 10–10<sup>3</sup> times more intense than both isolated and oligomeric species [37,38]. Hence, the relatively weak intensity of crystalline MoO<sub>3</sub> bands suggests that oligomeric MoO<sub>x</sub> domains are predominant on these catalysts. Further, the absence of bands at 745 and 1000 cm<sup>-1</sup> for MoO<sub>3</sub>/ZrO<sub>2</sub>; 822, 890, and 915 cm<sup>-1</sup> for MoO<sub>3</sub>/ $\gamma$ -Al<sub>2</sub>O<sub>3</sub>; and 320, 380, 910, and 955 cm<sup>-1</sup> for MoO<sub>3</sub>/CeO<sub>2</sub> indicates that crystalline heterometallic molybdates, such as Zr(MoO<sub>4</sub>)<sub>2</sub>, Al<sub>2</sub>(MoO<sub>4</sub>)<sub>3</sub>, and Ce<sub>2</sub>Mo<sub>4</sub>O<sub>15</sub>, are not formed on the catalyst surface [39–42]. MoO<sub>3</sub>/ZrO<sub>2</sub> has bands at ca. 810, 865, 950, and 980 cm<sup>-1</sup>. The latter two have been assigned to  $\bar{\nu}$  (Mo=O) for oligomeric MoO<sub>x</sub> domains [38,40]. The bands at ca. 810 and 865 cm<sup>-1</sup> have been assigned to either oligomeric  $\bar{\nu}_{\text{antisymmetric}}$  (Mo–O–Mo) and/or  $\bar{\nu}_{\text{antisymmetric}}$  (Mo–O–Zr) [40]. The presence of two bands for  $\bar{\nu}$  (Mo=O) may also suggest the existence of two different species that were not observed for other supported catalysts. Similarly, the  $\bar{\nu}_{\text{deformation}}$  (Mo–O–Mo) band at ca. 220 cm<sup>-1</sup> for both MoO<sub>3</sub>/SiO<sub>2</sub> and MoO<sub>3</sub>/ $\gamma$ -Al<sub>2</sub>O<sub>3</sub>, the  $\bar{\nu}_{\text{bending}}$  (Mo–O–Mo) band at ca. 340 and 380 cm<sup>-1</sup> for MoO<sub>3</sub>/ $\gamma$ -Al<sub>2</sub>O<sub>3</sub> and MoO<sub>3</sub>/SiO<sub>2</sub>, respectively, and the  $\bar{\nu}$  (Mo=O) band at ca. 950 cm<sup>-1</sup> for both MoO<sub>3</sub>/SiO<sub>2</sub> and MoO<sub>3</sub>/ $\gamma$ -Al<sub>2</sub>O<sub>3</sub>, can all be attributed to oligomeric MoO<sub>x</sub> domains. The presence of  $\bar{\nu}$  (Mo=O) bands at ca. 940 and 990 cm<sup>-1</sup> (dehydrated) for MoO<sub>3</sub>/CeO<sub>2</sub> and  $\bar{\nu}_{\text{antisymmetric}}$  (Mo–O–Mo) bands at ca. 880, and 800 cm<sup>-1</sup> for MoO<sub>3</sub>/SiO<sub>2</sub> and MoO<sub>3</sub>/CeO<sub>2</sub>, respectively, further confirm the oligomeric nature of MoO<sub>x</sub> domains [26,41,43–51]. Taken together, the PXRD and Raman spectroscopy data indicate that at loadings of 10 wt%, the MoO<sub>x</sub> domains are dispersed on the support surface mostly as oligomeric species, regardless of the support used.

### 3.2. Catalyst physical properties and redox-active site quantification

Physical properties of the supports and supported Mo catalysts used in this study, including surface area, oxygen uptake, and percentage of redox-active Mo species are summarized in Table 1. With the exception of MoO<sub>3</sub>/TiO<sub>2</sub>, the surface area of all catalysts reduced upon incorporation of dispersed Mo species on the support. The reduction in surface area may be attributed to the blockage of pores by larger MoO<sub>x</sub> domains [52,53]. The negligible change in surface area for TiO<sub>2</sub> upon dispersion of Mo species has also been reported by Tsilomelekis et al. [27]. MoO<sub>3</sub>/CeO<sub>2</sub> showed the largest reduction in surface area from 83.4 to 29.7 m<sup>2</sup>/g (64.4%), which is also consistent with previous reports [54].

Oxygen chemisorption data show that MoO<sub>3</sub>/TiO<sub>2</sub> featured the highest oxygen uptake values (245.0  $\mu\text{mol/g}$ ), followed by MoO<sub>3</sub>/ZrO<sub>2</sub> (137.9  $\mu\text{mol/g}$ ), and MoO<sub>3</sub>/CeO<sub>2</sub> (131.0  $\mu\text{mol/g}$ ). MoO<sub>3</sub>/SiO<sub>2</sub> and MoO<sub>3</sub>/ $\gamma$ -Al<sub>2</sub>O<sub>3</sub> had much lower oxygen uptake values of 98.3 and 43.1  $\mu\text{mol/g}$ , respectively. Desikan et al. used oxygen uptake values to quantify the number of redox-active Mo

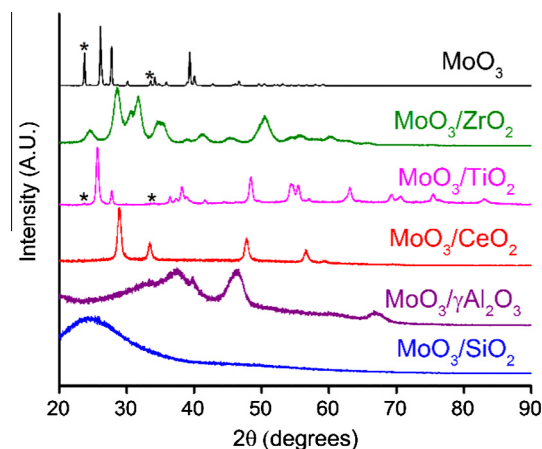


Fig. 1. Powder X-ray diffraction (PXRD) patterns of supported MoO<sub>3</sub> (10 wt%) catalysts normalized by maximum peak intensity for each catalyst.

species on the support surface, which differ based on the nature of interaction between Mo and support [55]. Reduction and chemisorption temperature of 623 K was used for all supported MoO<sub>3</sub> catalysts in accordance with the literature reports for quantifying O<sub>2</sub> uptake on MoO<sub>3</sub>/SiO<sub>2</sub>, MoO<sub>3</sub>/TiO<sub>2</sub>, MoO<sub>3</sub>/ZrO<sub>2</sub>, and MoO<sub>3</sub>/Nb<sub>2</sub>O<sub>5</sub> [52,53,55–57]. We note that the 623 K temperature used for reduction is close to 593 K used in our reactivity studies. The oxygen uptake values were used to determine the number of redox-active Mo species, allowing us to normalize HDO reactivity for all supported catalysts.

### 3.3. H<sub>2</sub>-temperature programmed reduction (TPR) of supported MoO<sub>3</sub> catalysts

Reducibility of supported catalysts was investigated by TPR (see Fig. 3). Control experiments of the bare supports show that, with the exception of CeO<sub>2</sub>, the supports do not show any appreciable H<sub>2</sub> consumption in the range of 573–873 K (Fig. S3, Supporting Information). Therefore, the observed maximum temperature of hydrogen consumption ( $T_{\text{max}}$ ) for the supported catalysts can be attributed to the reduction of dispersed octahedral Mo<sup>6+</sup> species to lower oxidation states [58]. MoO<sub>3</sub>/ZrO<sub>2</sub>, MoO<sub>3</sub>/TiO<sub>2</sub>, and MoO<sub>3</sub>/ $\gamma$ -Al<sub>2</sub>O<sub>3</sub> featured significantly lower  $T_{\text{max}}$  values of ca. 680, 710, and 685 K, respectively. Further, MoO<sub>3</sub>/ZrO<sub>2</sub> has an additional peak at ca. 725 K, which may suggest the presence of two different Mo species, in agreement with the two bands for  $\bar{\nu}$  (Mo=O) observed in the Raman spectrum (Fig. 2(b)). On the other hand, MoO<sub>3</sub>/SiO<sub>2</sub>, and MoO<sub>3</sub>/CeO<sub>2</sub> show higher  $T_{\text{max}}$  values of ca. 790 and 810 K, respectively. The  $T_{\text{max}}$  values for all catalysts agree well with the literature values reported for the similar loadings of MoO<sub>3</sub> on these supports [36,48,57–59]. Bulk MoO<sub>3</sub> has  $T_{\text{max}}$  values at 995, 1050, and 1090 K (Fig. S4, Supporting Information), with first two peaks corresponding to the reduction of MoO<sub>3</sub> to MoO<sub>2</sub>, and the minor last peak corresponding to conversion of MoO<sub>3</sub> to Mo<sub>4</sub>O<sub>11</sub> [57,60]. This progression is consistent with previous studies showing the formation of MoO<sub>2</sub> before Mo<sub>4</sub>O<sub>11</sub> [61]. These  $T_{\text{max}}$  values are considerably higher than those observed for the supported catalysts as they correspond to bulk phase transformations [52].

### 3.4. Diffuse reflectance UV–Visible (DR UV–Vis) spectroscopy

The local structure of Mo (VI) species was probed with UV–Vis spectroscopy, focusing on ligand-to-metal charge transfer (LMCT) transitions (Figs. S5 and S6, Supporting Information) and their corresponding absorption-edge energies ( $E_g$ ) (Table 2). From the five supports used in the study, ZrO<sub>2</sub>, TiO<sub>2</sub>, and CeO<sub>2</sub> absorb strongly

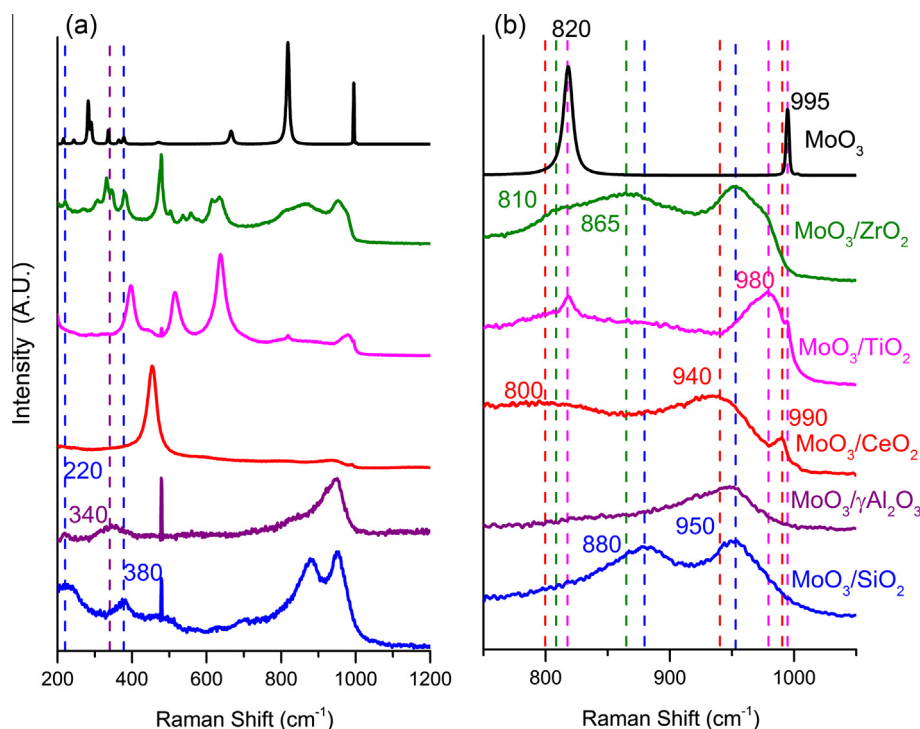


**Fig. 2.** Raman spectra of supported MoO<sub>3</sub> (10 wt%) catalysts in the Raman shift ranges of (a) 200–1200 cm<sup>-1</sup> and (b) 750–1050 cm<sup>-1</sup> normalized by maximum peak intensities for each catalyst in each range. The band at 480 cm<sup>-1</sup> is due to the glass slide used as a base for holding catalyst samples.

**Table 1**  
Textural properties and oxygen chemisorption values for supported MoO<sub>3</sub> catalysts.

Catalyst (10 wt% nominal loading)	BET surface area of support (m <sup>2</sup> /g)	BET surface area of catalyst (m <sup>2</sup> /g)	Oxygen uptake <sup>a</sup> (μmol/g)	Redox-active Mo species <sup>b</sup> (%)
MoO <sub>3</sub> /ZrO <sub>2</sub>	137.9	117.3	137.9	39.7
MoO <sub>3</sub> /TiO <sub>2</sub>	54.0	54.0	245.0	70.6
MoO <sub>3</sub> /CeO <sub>2</sub>	83.4	29.7	131.0	37.7
MoO <sub>3</sub> /γAl <sub>2</sub> O <sub>3</sub>	239.2	223.3	43.1	12.4
MoO <sub>3</sub> /SiO <sub>2</sub>	360.0	268.8	98.3	28.3

<sup>a</sup>  $T_{\text{reduction}} = T_{\text{chemisorption}} = 623$  K.

<sup>b</sup> Calculated as given in Eq. (7).

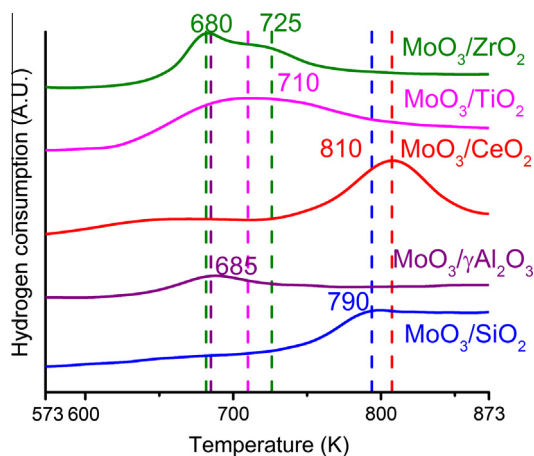


**Fig. 3.** Hydrogen consumption during temperature programmed reduction (TPR) of supported MoO<sub>3</sub> (10 wt%) catalysts. Calcination with O<sub>2</sub> at 773 K for 2 h. TPR conditions: 1% H<sub>2</sub> flow rate = 50 ml min<sup>-1</sup>, ramp = 2 K min<sup>-1</sup>. Mass of supported catalyst = 400 mg.

in the UV–Vis region in decreasing order of absorption-edge energies (Table 2), and overlap with LMCT transitions for Mo (VI) species (O<sup>2-</sup> → Mo<sup>6+</sup>) in the wavelength range of 200–600 nm (Fig. S5 (a)) [62]. Both SiO<sub>2</sub> and γAl<sub>2</sub>O<sub>3</sub> are weak absorbers in the UV–Vis region, and their absorption can therefore be neglected (Fig. S5 (b)). Although bands corresponding to LMCT transitions of supported molybdenum (VI) species are broad and do not provide definite structural information [44], recent studies have used the absorption-edge energies of these LMCT transitions to provide quantitative information on the local structures of Mo (VI) species [34,51,63]. The  $E_g$  values for both MoO<sub>3</sub>/SiO<sub>2</sub> and MoO<sub>3</sub>/γAl<sub>2</sub>O<sub>3</sub> are 4.1 eV, consistent with the presence of sub-monolayer dispersed Mo species on these supports [64,65], and in agreement with both the observed PXRD patterns and the Raman spectra. For samples that feature LMCT transitions, all the absorption-edge energies shift to lower values upon incorporation of molybdenum (VI) species. For instance, MoO<sub>3</sub>/ZrO<sub>2</sub> has an  $E_g$  value of 3.6 eV, as compared to 5.1 eV for the bare support. This shift is attributed to the presence of oligomeric MoO<sub>x</sub> domains on the surface [21,51]. Note that LMCT transitions for support cations and Mo (VI) species do not significantly overlap for MoO<sub>3</sub>/ZrO<sub>2</sub>, allowing us to distinguish the edge energies of Mo (VI) and Zr (IV) species. The  $E_g$  values

**Table 2**Absorption-edge energy of supports and supported catalysts (10 wt%) determined from UV–Vis spectroscopy.<sup>a,b</sup>

Catalysts	Absorption edge energy of support (eV)	Absorption edge energy of supported catalyst (eV)
MoO <sub>3</sub> /ZrO <sub>2</sub>	5.1	3.6
MoO <sub>3</sub> /TiO <sub>2</sub>	3.6	3.3
MoO <sub>3</sub> /CeO <sub>2</sub>	3.3	3.1
MoO <sub>3</sub> /γAl <sub>2</sub> O <sub>3</sub>	n/d	4.1
MoO <sub>3</sub> /SiO <sub>2</sub>	n/d	4.1
MoO <sub>3</sub>	n/a	3.1

<sup>a</sup> n/d: not determined in the range of wavelength used in the study.<sup>b</sup> n/a: not applicable.

also decrease for MoO<sub>3</sub>/TiO<sub>2</sub> and MoO<sub>3</sub>/CeO<sub>2</sub> after incorporation of Mo (VI) species, but not as drastically as for MoO<sub>3</sub>/ZrO<sub>2</sub>. The smaller difference in  $E_g$  values for these supported catalysts and the corresponding bare supports may be due to the overlap between strong absorption by the support and the weak absorption by the Mo (VI) species, as previously observed for supported V<sub>2</sub>O<sub>5</sub> catalysts [66]. As such, it is difficult to deduce any insights on the local structure of Mo (VI) on these two materials.

### 3.5. Reactivity studies for comparison of HDO of *m*-cresol on supported MoO<sub>3</sub> catalysts

The product distributions obtained for all the supported catalysts are reported in Table 3 for  $T = 593$  K, a WHSV of 8.27 h<sup>-1</sup>, and a TOS = 3 h. On an equivalent MoO<sub>3</sub> mass basis, conversions for MoO<sub>3</sub>/ZrO<sub>2</sub> and MoO<sub>3</sub>/TiO<sub>2</sub> were 78% and 47%, respectively. In contrast, MoO<sub>3</sub>/CeO<sub>2</sub>, MoO<sub>3</sub>/γAl<sub>2</sub>O<sub>3</sub>, MoO<sub>3</sub>/SiO<sub>2</sub>, and bulk MoO<sub>3</sub> yielded conversions of 8%, 13%, 10%, and 13%, respectively. The selectivity to hydrocarbons exceeded 97% for MoO<sub>3</sub>/ZrO<sub>2</sub>, MoO<sub>3</sub>/TiO<sub>2</sub>, and MoO<sub>3</sub>/CeO<sub>2</sub>. On the other hand, MoO<sub>3</sub>/SiO<sub>2</sub> and MoO<sub>3</sub>/γAl<sub>2</sub>O<sub>3</sub> had lower selectivity values to hydrocarbons of 90% and 76%, respectively. Toluene was the only hydrocarbon product generated on all catalysts, except for MoO<sub>3</sub>/γAl<sub>2</sub>O<sub>3</sub>, which also generated phenol and dimethyl phenol. Products with ring saturation, such as methyl cyclohexane, were not observed for any catalyst. Taken together, these data indicate that the deoxygenation pathway on all catalysts involved a selective C–O bond cleavage rather than a pathway involving hydrogenation/dehydration as observed for supported noble metals [67], or sequential hydrogenation as observed for supported Mo<sub>2</sub>C [68]. The formation of dimethyl phenol on MoO<sub>3</sub>/γAl<sub>2</sub>O<sub>3</sub> may be attributed to transalkylation reactions promoted by acid sites present on the support [30,69]. Control experiments using bare supports showed no appreciable HDO activity for *m*-cresol, thereby confirming that reactivity arises from the

Mo species. Mass balances coupled with gravimetric analyses suggest that less than 1% of the total carbon fed is either transformed to soft coke or incorporated into the MoO<sub>x</sub> lattice as carbidic or oxycarbidic species (Table 3), as previously reported for bulk MoO<sub>3</sub> [14]. Our data do not allow us to differentiate the carbon in soft coke from the carbon that may be incorporated into the MoO<sub>x</sub> domains.

A comparison of initial rates for conversion of *m*-cresol to toluene is presented in Fig. 4. Rates are normalized in three different ways: (a) per unit mass of MoO<sub>3</sub>, (b) per total surface area, and (c) per number of oxygen-uptake sites, as described in Eq. (9). MoO<sub>3</sub>/ZrO<sub>2</sub> (~65 mmol h<sup>-1</sup> g<sub>MoO3</sub><sup>-1</sup>) and MoO<sub>3</sub>/TiO<sub>2</sub> (~68 mmol h<sup>-1</sup> g<sub>MoO3</sub><sup>-1</sup>) featured significantly higher specific rates than all other catalysts tested (Fig. 4(a)). Normalizing rates by surface area shows that MoO<sub>3</sub>/TiO<sub>2</sub> is the most active catalyst (~126 μmol h<sup>-1</sup> m<sup>-2</sup>), followed by MoO<sub>3</sub>/ZrO<sub>2</sub> (~55 μmol h<sup>-1</sup> m<sup>-2</sup>) and MoO<sub>3</sub>/CeO<sub>2</sub> (~40 μmol h<sup>-1</sup> m<sup>-2</sup>). Both MoO<sub>3</sub>/SiO<sub>2</sub> and MoO<sub>3</sub>/γAl<sub>2</sub>O<sub>3</sub> displayed rates lower than 5 μmol h<sup>-1</sup> m<sup>-2</sup>. We note that although MoO<sub>3</sub>/TiO<sub>2</sub> has higher initial rates, it features a more abrupt initial deactivation, leading to lower conversions than MoO<sub>3</sub>/ZrO<sub>2</sub> after 1 h on stream, at an equivalent WHSV (see Fig. S7, Supporting Information). STY data show a reactivity trend of MoO<sub>3</sub>/ZrO<sub>2</sub> > MoO<sub>3</sub>/TiO<sub>2</sub> > MoO<sub>3</sub>/γAl<sub>2</sub>O<sub>3</sub> ≫ MoO<sub>3</sub>/SiO<sub>2</sub> > MoO<sub>3</sub>/CeO<sub>2</sub> (see Fig. 4c). After 2 h on stream, the reactivity trend changes to MoO<sub>3</sub>/ZrO<sub>2</sub> > MoO<sub>3</sub>/γAl<sub>2</sub>O<sub>3</sub> > MoO<sub>3</sub>/TiO<sub>2</sub> ≫ MoO<sub>3</sub>/SiO<sub>2</sub> > MoO<sub>3</sub>/CeO<sub>2</sub>, due to mainly the fast initial deactivation of MoO<sub>3</sub>/TiO<sub>2</sub> (Fig. S8, Supporting Information).

### 3.6. Post-reaction catalyst characterization

#### 3.6.1. PXRD and XPS of spent catalysts

PXRD patterns of spent catalysts (TOS = 7.5 h) only show appreciable structural changes for bulk MoO<sub>3</sub> and MoO<sub>3</sub>/TiO<sub>2</sub> (Fig. S9, Supporting Information). Indeed, the phase-transformation of bulk MoO<sub>3</sub> into a mixture of MoO<sub>2</sub> and molybdenum oxycarbohydride (Mo<sub>x</sub>C<sub>y</sub>H<sub>z</sub>) has been previously reported by Prasomsri et al. [14]. For MoO<sub>3</sub>/TiO<sub>2</sub>, it is observed that the peaks at  $2\theta = 23.7^\circ$  and  $34.2^\circ$ , corresponding to crystalline MoO<sub>3</sub> nanoparticles, disappear after reaction. However, the formation of bulk molybdenum oxycarbohydride (Mo<sub>x</sub>C<sub>y</sub>H<sub>z</sub>) is not detected for the spent MoO<sub>3</sub>/TiO<sub>2</sub> catalysts, indicating that bulk transformations of either unsupported nanoparticles or surface MoO<sub>x</sub> domains to Mo<sub>x</sub>C<sub>y</sub>H<sub>z</sub> cannot be detected with PXRD. Note that the peaks corresponding to MoO<sub>2</sub> overlap with TiO<sub>2</sub> peaks and cannot be resolved.

XPS spectra were acquired on the post-reaction samples (TOS = 7.5 h) to probe the final oxidation states of the surface Mo species (Fig. 5). XPS spectra of pre-reaction samples show the pres-

**Table 3**Reactivity data for the conversion of *m*-cresol on bulk and supported MoO<sub>3</sub> (10 wt%) catalysts<sup>a</sup> at TOS = 3 h.

Catalysts	MoO <sub>3</sub> /ZrO <sub>2</sub>	MoO <sub>3</sub> /TiO <sub>2</sub>	MoO <sub>3</sub> /CeO <sub>2</sub>	MoO <sub>3</sub> /γAl <sub>2</sub> O <sub>3</sub>	MoO <sub>3</sub> /SiO <sub>2</sub>	MoO <sub>3</sub>
Conversion (C-mol%)	78	47	8	13	10	13
Selectivity to hydrocarbons	99	99	97	76	90	99
Yield (C-mol%)						
Hydrocarbons						
Benzene	0	0	0	0	0	0
Toluene	77	46	7	10	9	13
Xylene	0	0	0	0	0	0
Oxygenates						
Phenol	0	0	0	1	0	0
<i>m</i> -Cresol	22	53	93	87	90	87
Dimethyl phenol	0	0	0	1	0	0
Carbon deposition <sup>b</sup>	<1	<1	<1	1	1	<1

<sup>a</sup> Reaction conditions:  $T = 593$  K,  $P_{\text{Total}} = 1.013$  bar ( $0.0102 P_{\text{Feed}}$ , balance H<sub>2</sub>), WHSV = 8.27 h<sup>-1</sup>, TOS = 3 h.<sup>b</sup> Carbon deposition estimated by TPO-MS on spent catalysts at TOS = 7.5 h.

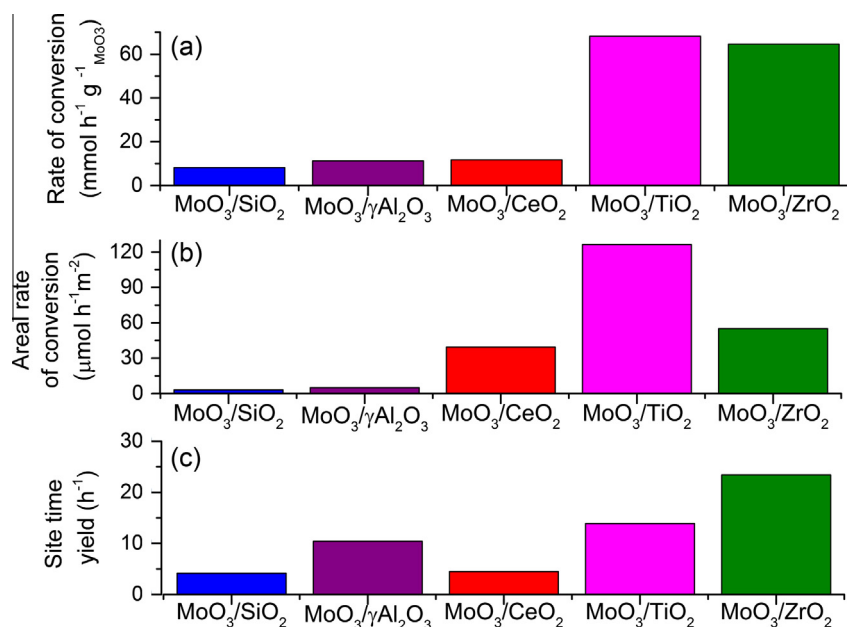


**Fig. 4.** Initial rates of toluene production for supported MoO<sub>3</sub> catalysts (10 wt%). (a) Rate of conversion normalized by unit mass of MoO<sub>3</sub> (mmol h<sup>-1</sup> g<sub>MoO<sub>3</sub></sub><sup>-1</sup>), (b) areal rate of conversion normalized by catalyst surface area (μmol h<sup>-1</sup> m<sup>-2</sup>), and (c) site time yield (h<sup>-1</sup>). Reaction conditions: T = 593 K, P<sub>Total</sub> = 1.013 bar (0.0102 P<sub>Feed</sub>, balance H<sub>2</sub>), WHSV = 8.27 h<sup>-1</sup>.

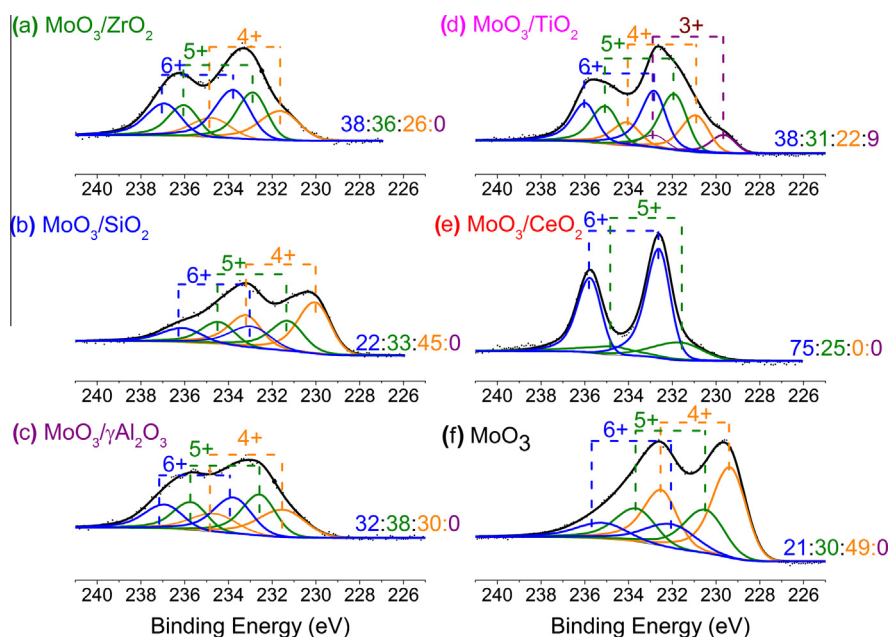


**Fig. 5.** XPS analysis showing the Mo (3d) energy region of the spent catalysts at time on stream (TOS) = 7.5 h. The ratios displayed correspond to the proportion of oxidation states of Mo<sup>6+</sup>, Mo<sup>5+</sup>, Mo<sup>4+</sup>, and Mo<sup>3+</sup>, respectively. Reaction conditions: T = 593 K, P<sub>Total</sub> = 1.013 bar (0.0102 P<sub>Feed</sub>, balance H<sub>2</sub>), WHSV = 8.27 h<sup>-1</sup>.

ence of only Mo<sup>6+</sup> species. However, the presence of reduced Mo species (Mo<sup>5+</sup> and Mo<sup>4+</sup>) is seen across all samples. MoO<sub>3</sub>/CeO<sub>2</sub> shows the highest proportion of Mo<sup>6+</sup> species (75%), with the remainder present as Mo<sup>5+</sup> species (25%). The proportion of Mo<sup>5+</sup> species ranges from 30% to 40% in all other samples. In addition, MoO<sub>3</sub>/TiO<sub>2</sub> features a unique Mo<sup>3+</sup> species (9%), based on the assignment of binding energies used by Choi and Thompson [70]. Importantly, only ca. 25% of the surface is reduced to Mo<sup>4+</sup> species for MoO<sub>3</sub>/ZrO<sub>2</sub>, MoO<sub>3</sub>/TiO<sub>2</sub>, and MoO<sub>3</sub>/γ-Al<sub>2</sub>O<sub>3</sub>, whereas ca. 50% of surface Mo species exist as Mo<sup>4+</sup> in bulk MoO<sub>3</sub> and MoO<sub>3</sub>/SiO<sub>2</sub> after reaction. XPS spectra acquired on another independent set of

supported MoO<sub>3</sub> samples demonstrate the reproducibility of this trend (Fig. S10, Supporting Information).

### 3.6.2. Temperature programmed oxidation studies

TPO-MS was performed on the spent catalysts (TOS = 7.5 h) to determine the nature and quantity of carbonaceous species on the catalyst surface (Fig. 6). The CO<sub>2</sub> evolution profile for MoO<sub>3</sub>/ZrO<sub>2</sub>, MoO<sub>3</sub>/CeO<sub>2</sub>, and MoO<sub>3</sub>/TiO<sub>2</sub> occurred in a temperature range between 570 and 750 K, similar to that of bulk MoO<sub>3</sub>. As such, we posit that the nature of the carbonaceous deposits on these catalyst surfaces is similar and can be attributed to the presence of “soft

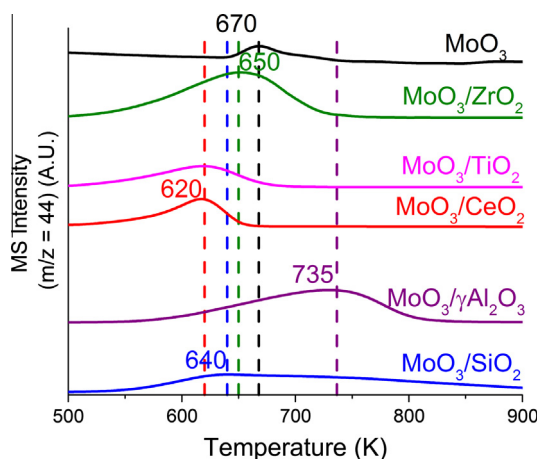


**Fig. 6.** Evolution of  $\text{CO}_2$  ( $m/z = 44$ ) as a function of temperature for spent catalysts measured by TPO-MS. TPO-MS conditions: 1%  $\text{O}_2$  flow rate =  $20 \text{ ml min}^{-1}$ . Ramp =  $7.5 \text{ K min}^{-1}$ . Mass of catalyst = 20–70 mg. Reaction conditions:  $T = 593 \text{ K}$ ,  $P_{\text{Total}} = 1.013 \text{ bar}$  ( $0.0102 \text{ bar } P_{\text{Feed}}$ , balance  $\text{H}_2$ ),  $\text{WHSV} = 8.27 \text{ h}^{-1}$ ,  $\text{TOS} = 7.5 \text{ h}$ .

coke”, as reported previously for spent  $\text{MoO}_3$  catalysts [14].  $\text{MoO}_3/\gamma\text{Al}_2\text{O}_3$  evolves  $\text{CO}_2$  at temperatures greater than 735 K, which can be ascribed to the presence of more refractory graphitic coke. A similar analysis for  $\text{MoO}_3/\text{SiO}_2$  reveals maximum  $\text{CO}_2$  evolution at 640 K, along with a long shoulder that continues beyond 850 K, thus suggesting the presence of both soft coke and graphitic coke. Regeneration of  $\text{MoO}_3/\gamma\text{Al}_2\text{O}_3$  and  $\text{MoO}_3/\text{SiO}_2$  would require calcination temperatures above 750 K, whereas all other supported catalysts would require calcination temperatures below 650 K. The TPO-MS data show that the carbon content of post-reaction  $\text{MoO}_3$ ,  $\text{MoO}_3/\text{SiO}_2$ ,  $\text{MoO}_3/\gamma\text{Al}_2\text{O}_3$ ,  $\text{MoO}_3/\text{CeO}_2$ ,  $\text{MoO}_3/\text{TiO}_2$ , and  $\text{MoO}_3/\text{ZrO}_2$  is 5.4, 4.7, 4.9, 0.7, 1.7, and 3.1% of the catalyst weight, respectively. We note that these values may include carbon incorporated into the lattice for any oxycarbide species formed during reaction [14].

### 3.7. Catalyst stability and regenerability

The catalysts with higher reactivity,  $\text{MoO}_3/\text{ZrO}_2$  and  $\text{MoO}_3/\text{TiO}_2$ , were selected for long-term stability studies. The supported catalysts were tested over 100 h and were compared with bulk  $\text{MoO}_3$  at space velocities that yielded similar conversion values (Fig. 7). Overall, the supported  $\text{MoO}_3$  catalysts featured a considerably enhanced stability when compared to bulk  $\text{MoO}_3$ . Specifically, bulk  $\text{MoO}_3$  undergoes a 2 h induction period in which conversion increases from 65% to 100%, followed by fast deactivation from a 100% conversion to less than 10% after 70 h [14]. A first-order deactivation profile can be divided into three zones with deactivation rate constants  $0.317$ ,  $0.085$ , and  $0.026 \text{ h}^{-1}$  for TOS ranges of 4–8.5, 8.5–24, and 24–70 h, respectively (Fig. S11, Supporting Information). In contrast,  $\text{MoO}_3/\text{ZrO}_2$  and  $\text{MoO}_3/\text{TiO}_2$  showed no induction period, featured lower initial deactivation rate constants than bulk  $\text{MoO}_3$ , and eventually reached a steady-state with drastically lower deactivation rate constants. Specifically, for  $\text{MoO}_3/\text{TiO}_2$ , m-cresol conversion decreased from 70% to 34% after the first 14.5 h on stream, with two deactivation zones that had first-order deactivation rate constants of  $0.305$  and  $0.039 \text{ h}^{-1}$  between TOS values of 0–2 and 2–14.5 h, respectively. Next, a stable period is observed in which conversion only decreased from 34% to 20% in the time range of 14.5 to 100 h, which translates to a deactivation rate constant of  $0.006 \text{ h}^{-1}$ . For  $\text{MoO}_3/\text{ZrO}_2$ , a decrease in m-cresol conversion from 90% to 62% is observed over the first 5.5 h, followed by gradual deactivation from 62% to 25% over the next 94.5 h, with first-order deactivation rate constants of  $0.197$  and  $0.013 \text{ h}^{-1}$ , respectively. The total site yields (defined as the

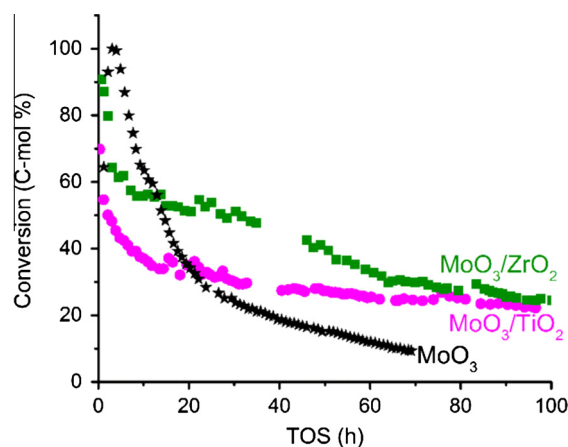


**Fig. 7.** Reactivity data of m-cresol HDO to toluene for time on stream (TOS) = 100 h, on  $\text{MoO}_3/\text{ZrO}_2$ ,  $\text{MoO}_3/\text{TiO}_2$ , and bulk  $\text{MoO}_3$  catalysts. Reaction conditions:  $T = 593 \text{ K}$ ,  $P_{\text{Total}} = 1.013 \text{ bar}$  ( $0.0102 \text{ bar } P_{\text{Feed}}$ , balance  $\text{H}_2$ ),  $\text{WHSV} = 8.27 \text{ h}^{-1}$  for supported catalysts,  $2.06 \text{ h}^{-1}$  for bulk  $\text{MoO}_3$ .

total moles of toluene formed per mole of redox-active Mo species over the course of the reaction) after 100 h for  $\text{MoO}_3/\text{TiO}_2$  and  $\text{MoO}_3/\text{ZrO}_2$  are ca. 440 and 1125, respectively (Fig. S12, Supporting Information). XPS analysis of the spent catalysts shows that the  $\text{Mo}^{6+}$  species in bulk  $\text{MoO}_3$  are reduced to  $\text{Mo}^{4+}$  and  $\text{Mo}^0$ , with no  $\text{Mo}^{6+}$  peaks left after 70 h on stream (Fig. 8). The C 1s spectra do not show any peaks associated with carbide carbon (Fig. S13, Supporting Information). However, the peaks corresponding to adventitious carbon may subsume the carbide carbon peak; hence, we cannot completely rule out the formation of  $\text{Mo}_2\text{C}$ . The deactivation of bulk  $\text{MoO}_3$  seems to be the result of surface over-reduction to  $\text{MoO}_2$  ( $\text{Mo}^{4+}$ ) and metallic Mo ( $\text{Mo}^0$ ). In contrast, Mo species appear to be stabilized in intermediate  $\text{Mo}^{5+}$  and  $\text{Mo}^{4+}$  oxidation states for  $\text{MoO}_3/\text{ZrO}_2$  and  $\text{MoO}_3/\text{TiO}_2$ . We note that the spent  $\text{MoO}_3/\text{TiO}_2$  catalyst also contains peaks associated with  $\text{Mo}^{3+}$  species.

Both  $\text{MoO}_3/\text{ZrO}_2$  and  $\text{MoO}_3/\text{TiO}_2$  can be regenerated by calcination under  $\text{O}_2$  ( $100 \text{ ml min}^{-1}$ ) at 673 K for 6 h (Fig. 9). While  $\text{MoO}_3/\text{TiO}_2$  has almost identical deactivation rate constants pre- and post-regeneration ( $0.290$  and  $0.305 \text{ h}^{-1}$  for fresh and regenerated catalysts, respectively), the initial deactivation rate is 2.75 times higher post-regeneration for  $\text{MoO}_3/\text{ZrO}_2$  (Fig. S14, Supporting Information). Nonetheless, the conversions seem to reach similar steady-state values for the regenerated catalysts. Taken together, the evolution of  $\text{CO}_2$  below 673 K during TPO-MS of spent  $\text{MoO}_3/\text{TiO}_2$  and  $\text{MoO}_3/\text{ZrO}_2$ , and their regenerated activity after calcination at 673 K indicates that the deactivation is reversible, and likely caused by carbonaceous deposits [68,71] and reduction of Mo species to oxidation states with low reactivity (e.g.,  $\text{Mo}^{4+}$ ) [14].

## 4. Discussion

Reduction of supported molybdenum catalysts has been shown to create coordinatively unsaturated (CU) sites that are active for hydrogenation and hydrodesulfurization (HDS) reactions [72]. In addition, for oxidative desulfurization and vapor-phase ammoxidation of 3-picoline to nicotinonitrile, an increase in oxygen chemisorption values was correlated with an increase in activity for supported  $\text{MoO}_3$  and  $\text{V}_2\text{O}_5$  catalysts with CU sites [52,53,60,73]. Past studies for sub-monolayer supported  $\text{MoO}_3$  catalysts have considered all surface Mo species to be active when calculating turnover frequencies or STYs for oxidation reactions [25,28,58,59,74]. However, we show that a different number of initial redox-active species calculated from oxygen chemisorption are

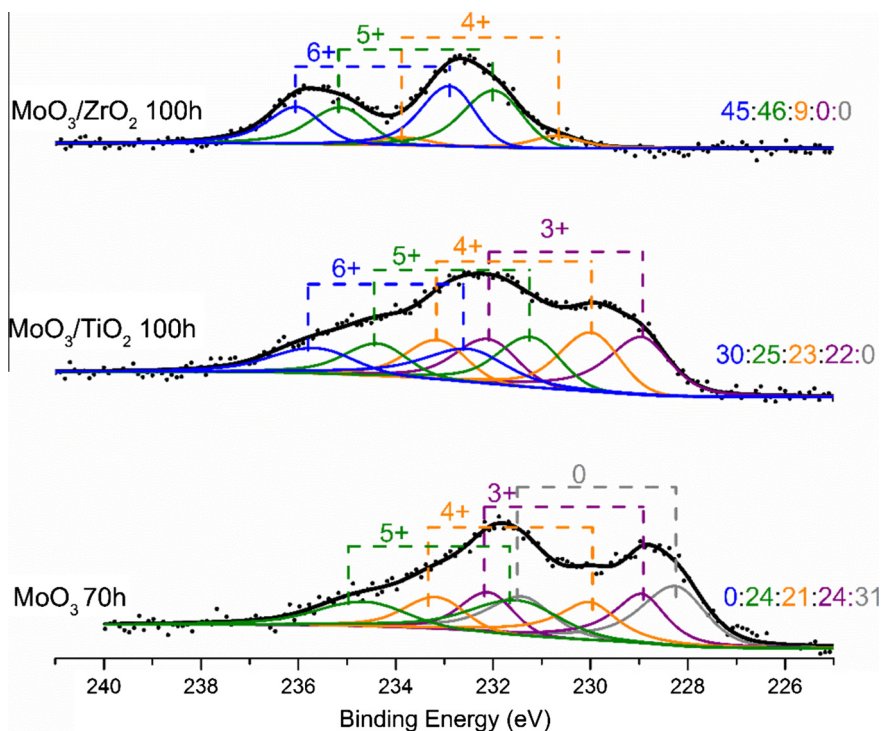


**Fig. 8.** XPS of the Mo (3d) energy region of the spent catalysts at time on stream (TOS) = 100 h for  $\text{MoO}_3/\text{ZrO}_2$  and  $\text{MoO}_3/\text{TiO}_2$ , and 70 h for bulk  $\text{MoO}_3$ . The ratios displayed correspond to proportion of oxidation states of  $\text{Mo}^{6+}$ ,  $\text{Mo}^{5+}$ ,  $\text{Mo}^{4+}$ ,  $\text{Mo}^{3+}$ , and  $\text{Mo}^0$  respectively. Reaction conditions:  $T = 593 \text{ K}$ ,  $P_{\text{Total}} = 1.013 \text{ bar}$  (0.0102 bar  $P_{\text{Feed}}$ , balance  $\text{H}_2$ ),  $\text{WHSV} = 8.27 \text{ h}^{-1}$  for supported catalysts,  $2.06 \text{ h}^{-1}$  for bulk  $\text{MoO}_3$ .

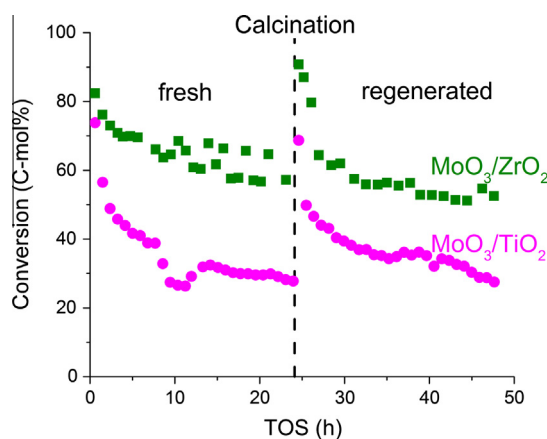


**Fig. 9.** Reactivity data for  $\text{MoO}_3/\text{ZrO}_2$  and  $\text{MoO}_3/\text{TiO}_2$  before and after calcination, during the HDO of *m*-cresol to toluene. Reaction conditions:  $T = 593 \text{ K}$ ,  $P_{\text{Total}} = 1.013 \text{ bar}$  (0.0102 bar  $P_{\text{Feed}}$ , balance  $\text{H}_2$ ),  $\text{WHSV} = 8.27 \text{ h}^{-1}$ . Regeneration conditions:  $T = 673 \text{ K}$ , 100%  $\text{O}_2$  for 6 h.

observed based on the nature of the support (Table 1). Thus, in contrast to previous studies, the STY values reported here account for the differences in number of redox-active Mo species.

Our previous work on HDO reactions using bulk  $\text{MoO}_3$  indicated that the reaction could proceed via an oxygen vacancy driven mechanism [13]. We hypothesize that HDO on supported molybdenum catalysts may occur via a similar mechanism, as illustrated in Scheme S1 (Supporting Information). Elucidation of reaction mechanism for conversion of *m*-cresol to toluene on supported  $\text{MoO}_3$  catalysts is not the focus of this study. We note that recent studies by Bhan and co-workers on the HDO of anisole and acetone on  $\text{Mo}_2\text{C}$  strongly suggest that both metallic and Brønsted acid sites play important roles during reaction upon partial oxidation of the surface [75,76]. The reducibility of Mo species on the support

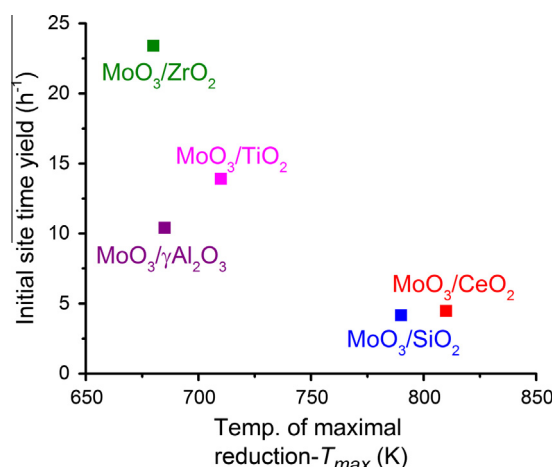


**Fig. 10.** Initial site time yield (STY) versus temperature of maximum reduction ( $T_{\text{max}}$ ) for supported  $\text{MoO}_3$  (10 wt%) on  $\text{SiO}_2$ ,  $\gamma\text{-Al}_2\text{O}_3$ ,  $\text{CeO}_2$ ,  $\text{TiO}_2$ , and  $\text{ZrO}_2$ . Reaction conditions:  $T = 593 \text{ K}$ ,  $P_{\text{Total}} = 1.013 \text{ bar}$  (0.0102 bar  $P_{\text{Feed}}$ , balance  $\text{H}_2$ ),  $\text{WHSV} = 8.27 \text{ h}^{-1}$ .

surface should influence the number of oxygen vacancies, and therefore change the reactivity toward HDO. The lower  $T_{\text{max}}$  values for  $\text{MoO}_3/\text{ZrO}_2$ ,  $\text{MoO}_3/\text{TiO}_2$ , and  $\text{MoO}_3/\gamma\text{-Al}_2\text{O}_3$  suggest higher reducibility (i.e., higher tendency to form CU Mo sites) on these supports. As such, the observed correlation between the lower  $T_{\text{max}}$  values with the higher STYs is expected (Fig. 10). The reducibility of dispersed species on support surface has been correlated with reactivity for other redox and vacancy driven reactions, including oxidation of methanol and ethanol, toluene hydrogenation, and oxidative dehydrogenation of propane [23,77–79].

Previous reports have shown that Au and Cu supported on  $\text{CeO}_2$  have higher acetylene and acetaldehyde oxidation activity than when supported on  $\text{ZrO}_2$  or  $\text{TiO}_2$  [80,81].  $\text{CeO}_2$  is known to be an “oxygen pump” capable of replenishing oxygen vacancies with

oxygen atoms from the bulk structure [82,83]. Accordingly, our data show that MoO<sub>3</sub>/CeO<sub>2</sub> featured the lowest reactivity for HDO, as Mo species are largely present in their highest oxidation (Mo<sup>6+</sup>) state (75%) and displayed high  $T_{max}$  values in the H<sub>2</sub>-TPR. We hypothesize that under the reaction conditions investigated, not enough CU Mo sites are created because they are quickly replenished with oxygen from the CeO<sub>2</sub> support. Indeed, migration of oxygen in CeO<sub>2</sub> has been shown to take place through a vacancy hopping mechanism [83]. Strong evidence supporting this mechanism is the measured increase in the proportion of Ce<sup>3+</sup> state in post-reaction samples (Fig. S15, Supporting Information), suggesting diffusion of oxygen from CeO<sub>2</sub> to the surface Mo species.

The prevalence of Mo<sup>5+</sup> species in most supported catalysts indicates the presence of CU sites. In bulk MoO<sub>3</sub>, Mo<sup>5+</sup> species arising from either the transformation of MoO<sub>3</sub> to MoO<sub>x</sub>C<sub>y</sub>H<sub>z</sub> or the reduction of MoO<sub>3</sub> to MoO<sub>3-x</sub> have been hypothesized to be responsible for HDO [14]. Although post-reaction PXRD analysis of supported catalysts showed no detectable crystalline oxycarbohydride formation, the presence of Mo<sup>5+</sup> species seems to relate to the reactivity. Recently, the presence of Mo<sup>5+</sup> species on thermally-reduced single-layer nanostructures of MoO<sub>3</sub> grown on Au (111) was attributed to one-dimensional shear defects formed by the elimination of bridging oxygen atoms [84]. As opposed to the over-reduction observed in bulk MoO<sub>3</sub>, the post-reaction XPS clearly shows the stabilization of Mo<sup>5+</sup> state for MoO<sub>3</sub>/ZrO<sub>2</sub>, as well as Mo<sup>3+</sup> and Mo<sup>5+</sup> states for MoO<sub>3</sub>/TiO<sub>2</sub> after 100 h on stream. Therefore, the increased stability of MoO<sub>3</sub>/ZrO<sub>2</sub> and MoO<sub>3</sub>/TiO<sub>2</sub> can be attributed to the stabilization of these intermediate Mo species upon dispersion of MoO<sub>3</sub> on these supports. Thus, the supports appear to play two key roles: on the one hand, the support allows for CU sites to be formed at lower temperatures (as evidenced by the H<sub>2</sub>-TPR data), and on the other, it prevents over-reduction to lower oxidation states with lower reactivity.

The differences in STY values across different catalysts suggest support-induced changes in intrinsic activity. With the exception of MoO<sub>3</sub>/CeO<sub>2</sub>, the STY values for HDO of m-cresol to toluene increase with decreasing electronegativity of the support cation (Fig. 11). The increasing reactivity with decreasing electronegativity of the support cation has been seen for supported catalysts in redox reactions, such as alcohol oxidation and oxidative dehydrogenation of alkanes [85–89]. For instance, the TOFs for monolayer-type supported MoO<sub>3</sub> catalysts for Mars-van Krevelen-type oxidative dehydrogenation of ethane followed a reactivity order of MoO<sub>3</sub>/ZrO<sub>2</sub> > MoO<sub>3</sub>/γAl<sub>2</sub>O<sub>3</sub> > MoO<sub>3</sub>/TiO<sub>2</sub> > MoO<sub>3</sub>/SiO<sub>2</sub> which was inversely correlated to the support cation electronegativity [27]. A decreasing cation support electronegativity (Si<sup>4+</sup> > Al<sup>3+</sup> > Ti<sup>4+</sup> > Zr<sup>4+</sup> > Ce<sup>4+</sup>) increases the electron density of the Mo–O–support bridging oxygen, improving catalytic activity for redox reactions [85,86]. This bond has also been reported to influence reactivity toward acidic products for supported niobium and tantalum oxide catalysts as seen by the inverse trend of increasing reactivity seen with increasing electronegativity of the support cation, due to increasing acidity of the Mo–O–support bridging oxygen [90]. In our case, we hypothesize that the Mo–O–support bridging oxygen atoms play an important role during H abstraction required to initiate the HDO process, similar to other redox reactions [89,91]. Increased reactivity for redox reactions has been ascribed to reduction in activation energy [27], and an increase in the pre-exponential factor on supports with more electropositive cations for oxidative dehydrogenation and alcohol oxidation reactions [85,86,88,89]. Quantum chemical calculations and near-edge X-ray absorption spectroscopy (NEXAFS) studies on oxidative dehydrogenation of methanol to formaldehyde also suggested that the higher reactivity of MoO<sub>3</sub> on TiO<sub>2</sub> and ZrO<sub>2</sub> compared to that on SiO<sub>2</sub> and Al<sub>2</sub>O<sub>3</sub> is correlated with the density of accessible electronic states, which ultimately

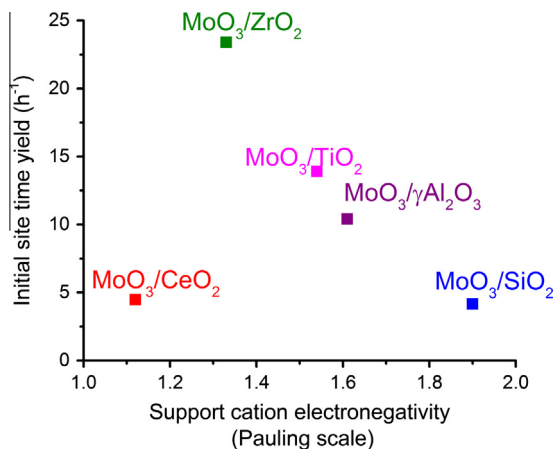


Fig. 11. Initial site time yield (STY) versus support cation electronegativity (Pauling scale) for supported MoO<sub>3</sub> (10 wt%) on SiO<sub>2</sub>, γAl<sub>2</sub>O<sub>3</sub>, CeO<sub>2</sub>, TiO<sub>2</sub>, and ZrO<sub>2</sub>. Reaction conditions: T = 593 K, P<sub>Total</sub> = 1.013 bar (0.0102 P<sub>Feed</sub>, balance H<sub>2</sub>), WHSV = 8.27 h<sup>-1</sup>.

influences the pre-exponential factor of the reaction rate constant [79,92]. The mechanistic origins for the increased reactivity for these redox reactions have been hypothesized to be due to a higher oxygenate steady-state equilibrium adsorption capacity and an easier H abstraction due to increased basicity of Mo–O–support bonds [27,85,86,88,89,92]. We posit that the genesis of the support's influence on HDO reactivity could be linked to these effects. Considering the electronegativity trend, MoO<sub>3</sub>/CeO<sub>2</sub> should have the highest unoccupied density of states of all catalysts tested, yet it features the lowest activity. As seen from both TPR and post-reaction XPS, the propensity for formation of oxygen vacancies is low on MoO<sub>3</sub>/CeO<sub>2</sub>. Computational studies on VO<sub>x</sub>/CeO<sub>2</sub> have indicated the role of CeO<sub>2</sub> in stabilizing the highest V<sup>5+</sup> state [91]. It is likely that a similar mechanism prevents the reduction of Mo<sup>6+</sup> to lower oxidation states, resulting in a decreased number of oxygenate adsorption sites. Overall, our results are consistent with an oxygen vacancy driven mechanism; however, other interpretations cannot be ruled out. Kinetic and in-situ titration studies will be crucial in determining the role of oxygen vacancy, metallic and Brønsted acid sites on bulk and supported MoO<sub>3</sub> catalysts for HDO.

The catalyst deactivation on MoO<sub>3</sub>/ZrO<sub>2</sub> and MoO<sub>3</sub>/TiO<sub>2</sub> is shown to be reversible, which is likely caused by coke deposition and reduction of Mo species to oxidation states with lower activity. The refractory coke formation on MoO<sub>3</sub>/γAl<sub>2</sub>O<sub>3</sub> and MoO<sub>3</sub>/SiO<sub>2</sub> is probably catalyzed by surface acidic sites [93]. The trend in the quantity of coke mirrors the trend in the acid strength of supports [94,95]. Indeed, γAl<sub>2</sub>O<sub>3</sub> is known to be a strongly acidic support, followed by TiO<sub>2</sub>, and ZrO<sub>2</sub> with weaker acidity [29,96]. The higher quantity and refractory nature of the graphitic coke formed on SiO<sub>2</sub> and γAl<sub>2</sub>O<sub>3</sub> makes them undesirable for use as supports for HDO.

## 5. Conclusions

In summary, the effect of metal oxide supports on redox behavior and intrinsic reactivity of Mo species toward HDO of m-cresol to toluene was investigated. All catalysts exhibit high toluene selectivity at a temperature of 593 K and low H<sub>2</sub> pressures (≤1 bar). Mo species are largely present as oligomeric domains on all supports. The intrinsic HDO activity of Mo species on different supports was compared by normalizing the rate of formation of toluene with the initial moles of redox-active Mo species, as determined by oxygen chemisorption. The catalytic activity toward HDO shows a strong dependence on the reducibility of surface Mo species and the electronegativity of support cation (with the exception of MoO<sub>3</sub>/CeO<sub>2</sub>). Our data show that TiO<sub>2</sub> and ZrO<sub>2</sub> are optimal sup-

ports that promote high activity and improved stability. The supports play an important role in stabilizing specific lower Mo oxidation states. Post-reaction characterization reveals a link between intermediate Mo ( $\text{Mo}^{5+}$  and  $\text{Mo}^{3+}$ ) states and catalytic activity. The XPS analysis on spent catalysts shows that  $\text{TiO}_2$  and  $\text{ZrO}_2$  stabilize  $\text{Mo}^{5+}$  species, in stark contrast to bulk  $\text{MoO}_3$ , which over-reduces to lower oxidation states with lower reactivity. Catalyst deactivation is reversible and likely caused by coke deposition and the reduction of Mo species to oxidation states with lower activity (e.g.,  $\text{Mo}^{4+}$ ). Both  $\text{MoO}_3/\text{ZrO}_2$  and  $\text{MoO}_3/\text{TiO}_2$  can be readily regenerated by calcination with  $\text{O}_2$  at 673 K.  $\text{MoO}_3/\text{SiO}_2$  and  $\text{MoO}_3/\gamma\text{Al}_2\text{O}_3$  exhibit a higher tendency to form refractory graphitic coke, thereby requiring higher calcination temperatures for regeneration. The mechanism of HDO is not conclusive, but reaction rates appear to be related to coordinatively unsaturated Mo sites, as required in an oxygen vacancy driven mechanism. Controlling the reducibility of dispersed active species, along with stabilizing intermediate oxidation states, is critical for developing active and robust oxide-based systems for the HDO of biomass-derived compounds.

## Acknowledgments

This research was funded by British Petroleum (BP) through the MIT Energy Initiative Advanced Conversion Research Program. The authors would like to thank Justin Nelson, for help with Raman spectroscopy.

## Appendix A. Supplementary material

Supplementary data associated with this article can be found, in the online version, at <http://dx.doi.org/10.1016/j.jcat.2015.07.034>.

## References

- [1] G.W. Huber, A. Corma, Synergies between bio- and oil refineries for the production of fuels from biomass, *Angew. Chem. Int. Ed.* 46 (2007) 7184–7201.
- [2] G.W. Huber, S. Iborra, A. Corma, Synthesis of transportation fuels from biomass: chemistry, catalysts, and engineering, *Chem. Rev.* 106 (2006) 4044–4098.
- [3] S. Czernik, A.V. Bridgwater, Overview of applications of biomass fast pyrolysis oil, *Energy Fuels* 18 (2004) 590–598.
- [4] Q. Zhang, J. Chang, T. Wang, Y. Xu, Review of biomass pyrolysis oil properties and upgrading research, *Energy Convers. Manage.* 48 (2007) 87–92.
- [5] H.Y. Zhang, Y.T. Cheng, T.P. Vispute, R. Xiao, G.W. Huber, Catalytic conversion of biomass-derived feedstocks into olefins and aromatics with ZSM-5: the hydrogen to carbon effective ratio, *Energy Environ. Sci.* 4 (2011) 2297–2307.
- [6] T.R. Carlson, G.A. Tompsett, W.C. Conner, G.W. Huber, Aromatic production from catalytic fast pyrolysis of biomass-derived feedstocks, *Top. Catal.* 52 (2009) 241–252.
- [7] J. Diebold, J. Scabill, Biomass to gasoline – upgrading pyrolysis vapors to aromatic gasoline with zeolite catalysis at atmospheric-pressure, *ACS Sym. Ser.* 376 (1988) 264–276.
- [8] N.E. Persson, S.D. Blass, C. Rosenthal, A. Bhan, L.D. Schmidt, On-line deoxygenation of cellulose pyrolysis vapors in a staged autothermal reactor, *RSC Adv.* 3 (2013) 20163–20170.
- [9] Q. Bu, H. Lei, A.H. Zacher, L. Wang, S. Ren, J. Liang, Y. Wei, Y. Liu, J. Tang, Q. Zhang, R. Ruan, A review of catalytic hydrodeoxygenation of lignin-derived phenols from biomass pyrolysis, *Bioresour. Technol.* 124 (2012) 470–477.
- [10] E. Furimsky, Hydroprocessing challenges in biofuels production, *Catal. Today* 217 (2013) 13–56.
- [11] H. Wang, J. Male, Y. Wang, Recent advances in hydrotreating of pyrolysis bio-oil and its oxygen-containing model compounds, *ACS Catal.* 3 (2013) 1047–1070.
- [12] M. Saidi, F. Samimi, D. Karimipourfard, T. Nimmanwudipong, B.C. Gates, M.R. Rahimpour, Upgrading of lignin-derived bio-oils by catalytic hydrodeoxygenation, *Energy Environ. Sci.* 7 (2014) 103.
- [13] T. Prasomsri, T. Nimmanwudipong, Y. Roman-Leshkov, Effective hydrodeoxygenation of biomass-derived oxygenates into unsaturated hydrocarbons by  $\text{MoO}_3$  using low  $\text{H}_2$  pressures, *Energy Environ. Sci.* 6 (2013) 1732–1738.
- [14] T. Prasomsri, M. Shetty, K. Murugappan, Y. Román-Leshkov, Insights into the catalytic activity and surface modification of  $\text{MoO}_3$  during the hydrodeoxygenation of lignin-derived model compounds into aromatic hydrocarbons under low hydrogen pressures, *Energy Environ. Sci.* 7 (2014) 2660.
- [15] P. Delporte, F. Meunier, C. Phamhuu, P. Venneques, M.J. Ledoux, J. Guille, Physical characterization of molybdenum oxycarbide catalyst – TEM, XRD and XPS, *Catal. Today* 23 (1995) 251–267.
- [16] C. Bouchy, C. Pham-Huu, B. Heinrich, C. Chaumont, M.J. Ledoux, Microstructure and characterization of a highly selective catalyst for the isomerization of alkanes: a molybdenum oxycarbide, *J. Catal.* 190 (2000) 92–103.
- [17] S. Damyanova, L. Petrov, P. Grange, XPS characterization of zirconium-promoted  $\text{CoMo}$  hydrodesulfurization catalysts, *Appl. Catal. A* 239 (2003) 241–252.
- [18] Q. Wang, J. Lu, Y. Chen, H. Guo, P. Cui, Effect of silica–alumina ratio on the performance of  $\text{K}_2\text{MoO}_4\text{-NiO/ZSM-5}$  in synthesis of methyl mercaptan from high  $\text{H}_2\text{S}$ -containing syngas, *Shiyu Huagong/Petrochem. Technol.* 43 (2014) 1014–1019.
- [19] H.F. Li, M.F. Li, Y. Chu, F. Liu, H. Nie, Effect of different preparation methods of  $\text{MoO}_3/\text{Al}_2\text{O}_3$  catalysts on the existing states of Mo species and hydrodesulfurization activity, *Fuel* 116 (2014) 168–174.
- [20] P. Gajardo, A. Mathieux, P. Grange, B. Delmon, Structure and catalytic activity of  $\text{CoMo}/\gamma\text{-Al}_2\text{O}_3$  and  $\text{CoMo}/\text{SiO}_2$  hydrodesulfurization catalysts: an xps and esr characterization of sulfided used catalysts, *Appl. Catal.* 3 (1982) 347–376.
- [21] G. Tsilomelekis, S. Boghosian, On the configuration, molecular structure and vibrational properties of  $\text{MoOx}$  sites on alumina, zirconia, titania and silica, *Catal. Sci. Technol.* 3 (2013) 1869.
- [22] T. Fievez, P. Geerlings, B.M. Weckhuysen, F. De Proft, Using DFT in search for support effects during methanol oxidation on supported molybdenum oxides, *ChemPhysChem* 12 (2011) 3281–3290.
- [23] K. Amakawa, L. Sun, C. Guo, M. Havecker, P. Kube, I.E. Wachs, S. Lwin, A.I. Frenkel, A. Patlolla, K. Hermann, R. Schlogl, A. Trunschke, How strain affects the reactivity of surface metal oxide catalysts, *Angew. Chem. Int. Ed.* 52 (2013) 13553–13557.
- [24] I.E. Wachs, Recent conceptual advances in the catalysis science of mixed metal oxide catalytic materials, *Catal. Today* 100 (2005) 79–94.
- [25] A. Christodoulakis, S. Boghosian, Molecular structure and activity of molybdena catalysts supported on zirconia for ethane oxidative dehydrogenation studied by operando Raman spectroscopy, *J. Catal.* 260 (2008) 178–187.
- [26] A. Christodoulakis, E. Heracleous, A. Lemonidou, S. Boghosian, An operando Raman study of structure and reactivity of alumina-supported molybdenum oxide catalysts for the oxidative dehydrogenation of ethane, *J. Catal.* 242 (2006) 16–25.
- [27] G. Tsilomelekis, A. Christodoulakis, S. Boghosian, Support effects on structure and activity of molybdenum oxide catalysts for the oxidative dehydrogenation of ethane, *Catal. Today* 127 (2007) 139–147.
- [28] G. Tsilomelekis, S. Boghosian, An operando Raman study of molecular structure and reactivity of molybdenum(VI) oxide supported on anatase for the oxidative dehydrogenation of ethane, *Phys. Chem. Chem. Phys.* 14 (2012) 2216–2228.
- [29] V.N. Bui, D. Laurenti, P. Delichère, C. Geantet, Hydrodeoxygenation of guaiacol Part II: Support effect for  $\text{CoMoS}$  catalysts on HDO activity and selectivity, *Appl. Catal. B* 101 (2011) 246–255.
- [30] D.A. Ruddy, J.A. Schaidle, J.R. Ferrell III, J. Wang, L. Moens, J.E. Hensley, Recent advances in heterogeneous catalysts for bio-oil upgrading via “ex situ catalytic fast pyrolysis”: catalyst development through the study of model compounds, *Green Chem.* 16 (2014) 454.
- [31] V.A. Yakovlev, S.A. Khromova, O.V. Sherstyuk, V.O. Dundich, D.Y. Ermakov, V.M. Novopashina, M.Y. Lebedev, O. Bulavchenko, V.N. Parmon, Development of new catalytic systems for upgraded bio-fuels production from bio-crude-oil and biodiesel, *Catal. Today* 144 (2009) 362–366.
- [32] Y. Wang, S. Van de Vyver, K.K. Sharma, Y. Roman-Leshkov, Insights into the stability of gold nanoparticles supported on metal oxides for the base-free oxidation of glucose to gluconic acid, *Green Chem.* 16 (2014) 719–726.
- [33] H.S. Fogler, *Essentials of Chemical Reaction Engineering*, 2011.
- [34] R.S. Weber, Effect of local structure on the UV–visible absorption edges of molybdenum oxide clusters and supported molybdenum oxides, *J. Catal.* 151 (1995) 470–474.
- [35] S. Brunauer, P.H. Emmett, E. Teller, Adsorption of gases in multimolecular layers, *J. Am. Chem. Soc.* 60 (1938) 309–319.
- [36] H. Zhu, M. Shen, Y. Wu, X. Li, J. Hong, B. Liu, X. Wu, L. Dong, Y. Chen, Dispersion behaviors of molybdena on titania (rutile and/or anatase), *J. Phys. Chem. B* 109 (2005) 11720–11726.
- [37] R. Radhakrishnan, C. Reed, S.T. Oyama, M. Seman, J.N. Kondo, K. Domen, Y. Ohminami, K. Asakura, Variability in the structure of supported  $\text{MoO}_3$  catalysts: studies using Raman and X-ray absorption spectroscopy with ab initio calculations, *J. Phys. Chem. B* 105 (2001) 8519–8530.
- [38] H. Liu, P. Cheung, E. Iglesia, Structure and support effects on the selective oxidation of dimethyl ether to formaldehyde catalyzed by  $\text{MoOx}$  domains, *J. Catal.* 217 (2003) 222–232.
- [39] H. Tian, I.E. Wachs, L.E. Briand, Comparison of UV and visible Raman spectroscopy of bulk metal molybdate and metal vanadate catalysts, *J. Phys. Chem. B* 109 (2005) 23491–23499.
- [40] I. Shupyk, J.Y. Piquemal, E. Briot, M.J. Vaulay, C. Connan, S. Truong, V. Zaitsev, F. Bozon-Verduraz, The use of low-nuclearity oxoperoxo molybdenum species to achieve high dispersions on zirconia materials, *Appl. Catal. A* 325 (2007) 140–153.

- [41] Y. Peng, R. Qu, X. Zhang, J. Li, The relationship between structure and activity of  $\text{MoO}_3\text{-CeO}_2$  catalysts for NO removal: influences of acidity and reducibility, *Chem. Commun.* 49 (2013) 6215–6217.
- [42] N. Al-Yassir, R. Le Van Mao, Physico-chemical properties of mixed molybdenum and cerium oxides supported on silica–alumina and their use as catalysts in the thermal-catalytic cracking (TCC) of *n*-hexane, *Appl. Catal. A* 305 (2006) 130–139.
- [43] N. Al-Yassir, R.L.V. Mao, Catalysts for the thermo-catalytic cracking (TCC) process: interactions between the yttria in yttria-doped alumina aerogel and the mono-oxide  $\text{MoO}_3$ ,  $\text{CeO}_2$ , and bi-oxide  $\text{MoO}_3\text{-CeO}_2$  species, *Appl. Catal. A* 332 (2007) 273–288.
- [44] K. Chen, S. Xie, A.T. Bell, E. Iglesia, Structure and properties of oxidative dehydrogenation catalysts based on  $\text{MoO}_3/\text{Al}_2\text{O}_3$ , *J. Catal.* 198 (2001) 232–242.
- [45] Y. Miao, G. Lu, X. Liu, Y. Guo, Y. Wang, Y. Guo, Effects of preparation procedure in sol–gel method on performance of  $\text{MoO}_3/\text{SiO}_2$  catalyst for liquid phase epoxidation of propylene with cumene hydroperoxide, *J. Mol. Catal. A: Chem.* 306 (2009) 17–22.
- [46] X. Du, L. Dong, C. Li, Y. Liang, Y. Chen, Diffuse reflectance infrared Fourier transform and Raman spectroscopic studies of  $\text{MoO}_3$  dispersed on  $\text{CeO}_2$  support, *Langmuir* 15 (1999) 1693–1697.
- [47] L. Dong, Y. Chen, The dispersion of molybdena on ceria, *J. Chem. Soc., Faraday Trans.* 92 (1996) 4589–4593.
- [48] H. Wan, D. Li, H. Zhu, Y. Zhang, L. Dong, Y. Hu, B. Liu, K. Sun, L. Dong, Y. Chen, A comparative study on the dispersion behaviors and surface acid properties of molybdena on  $\text{CeO}_2$  and  $\text{ZrO}_2$  (Tet), *J. Colloid Interface Sci.* 326 (2008) 28–34.
- [49] X. Du, L. Dong, C. Li, Y. Liang, Y. Chen, Vibrational spectroscopic studies of molybdena dispersed on ceria support, *Spectrosc. Lett.* 31 (1998) 441–457.
- [50] W. Yu, J. Zhu, L. Qi, C. Sun, F. Gao, L. Dong, Y. Chen, Surface structure and catalytic properties of  $\text{MoO}_3/\text{CeO}_2$  and  $\text{CuO}/\text{MoO}_3/\text{CeO}_2$ , *J. Colloid Interface Sci.* 364 (2011) 435–442.
- [51] H. Tian, C.A. Roberts, I.E. Wachs, Molecular structural determination of molybdena in different environments: aqueous solutions, bulk mixed oxides, and supported  $\text{MoO}_3$  catalysts, *J. Phys. Chem. C* 114 (2010) 14110–14120.
- [52] K.V.R. Chary, T. Bhaskar, G. Kishan, K.R. Reddy, Characterization and reactivity of molybdenum oxide catalysts supported on niobia, *J. Phys. Chem. B* 105 (2001) 4392–4399.
- [53] K.V.R. Chary, G. Kishan, T. Bhaskar, C. Sivaraj, Structure and reactivity of vanadium oxide catalysts supported on anatase  $\text{TiO}_2$ , *J. Phys. Chem. B* 102 (1998) 6792–6798.
- [54] H. Nasser, Á. Rédey, T. Yuzhakova, J. Kovács, Thermal stability and surface structure of  $\text{Mo}/\text{CeO}_2$  and Ce-doped  $\text{Mo}/\text{Al}_2\text{O}_3$  catalysts, *J. Therm. Anal. Calorim.* 95 (2009) 69–74.
- [55] A.N. Desikan, L. Huang, S.T. Oyama, Structure and dispersion of molybdenum oxide supported on alumina and titania, *J. Chem. Soc., Faraday Trans.* 88 (1992) 3357–3365.
- [56] A.N. Desikan, L. Huang, S.T. Oyama, Oxygen chemisorption and laser Raman spectroscopy of unsupported and silica-supported molybdenum oxide, *J. Phys. Chem.* 95 (1991) 10050–10056.
- [57] K.V.R. Chary, K.R. Reddy, G. Kishan, J.W. Niemantsverdriet, G. Mestl, Structure and catalytic properties of molybdenum oxide catalysts supported on zirconia, *J. Catal.* 226 (2004) 283–291.
- [58] Y. Cui, N. Liu, Y. Xia, J. Lv, S. Zheng, N. Xue, L. Peng, X. Guo, W. Ding, Efficient self-metathesis of 1-butene on molybdenum oxide supported on silica modified one-dimensional  $\gamma\text{-Al}_2\text{O}_3$ , *J. Mol. Catal. A: Chem.* 394 (2014) 1–9.
- [59] T. Hahn, U. Benstrup, M. Armbrüster, E.V. Kondratenko, D. Linke, The enhancing effect of Bronsted acidity of supported MoOx species on their activity and selectivity in ethylene/trans-2-butene metathesis, *ChemCatChem* 6 (2014) 1664–1672.
- [60] T. Bhaskar, K.R. Reddy, C.P. Kumar, M.R.V.S. Murthy, K.V.R. Chary, Characterization and reactivity of molybdenum oxide catalysts supported on zirconia, *Appl. Catal. A* 211 (2001) 189–201.
- [61] T. Ressler, R.E. Jentoft, J. Wienold, M.M. Gunter, O. Timpe, In situ XAS and XRD studies on the formation of Mo suboxides during reduction of  $\text{MoO}_3$ , *J. Phys. Chem. B* 104 (2000) 6360–6370.
- [62] M. Fournier, C. Louis, M. Che, P. Chaquin, D. Masure, Polyoxometallates as models for oxide catalysts: Part I. An UV–visible reflectance study of polyoxomolybdates: influence of polyhedra arrangement on the electronic transitions and comparison with supported molybdenum catalysts, *J. Catal.* 119 (1989) 400–414.
- [63] J. Scholz, A. Walter, A.H.P. Hahn, T. Ressler, Molybdenum oxide supported on nanostructured MgO: influence of the alkaline support properties on MoOx structure and catalytic behavior in selective oxidation, *Microporous Mesoporous Mater.* 180 (2013) 130–140.
- [64] S. Braun, L.G. Appel, V.L. Camorim, M. Schmal, Thermal spreading of  $\text{MoO}_3$  onto silica supports, *J. Phys. Chem. B* 104 (2000) 6584–6590.
- [65] Y. Lou, H. Wang, Q. Zhang, Y. Wang, SBA-15-supported molybdenum oxides as efficient catalysts for selective oxidation of ethane to formaldehyde and acetaldehyde by oxygen, *J. Catal.* 247 (2007) 245–255.
- [66] X. Gao, I.E. Wachs, Investigation of surface structures of supported vanadium oxide catalysts by UV–vis–NIR diffuse reflectance spectroscopy, *J. Phys. Chem. B* 104 (2000) 1261–1268.
- [67] L. Nie, D.E. Resasco, Kinetics and mechanism of *m*-cresol hydrodeoxygenation on a  $\text{Pt}/\text{SiO}_2$  catalyst, *J. Catal.* 317 (2014) 22–29.
- [68] W.S. Lee, Z.S. Wang, R.J. Wu, A. Bhan, Selective vapor-phase hydrodeoxygenation of anisole to benzene on molybdenum carbide catalysts, *J. Catal.* 319 (2014) 44–53.
- [69] T. Nimmanwudipong, C. Aydin, J. Lu, R.C. Runnebaum, K.C. Brodwater, N.D. Browning, D.E. Block, B.C. Gates, Selective hydrodeoxygenation of guaiacol catalyzed by platinum supported on magnesium oxide, *Catal. Lett.* 142 (2012) 1190–1196.
- [70] J.-G. Choi, L. Thompson, XPS study of as-prepared and reduced molybdenum oxides, *Appl. Surf. Sci.* 93 (1996) 143–149.
- [71] W.S. Lee, Z.S. Wang, W.Q. Zheng, D.G. Vlachos, A. Bhan, Vapor phase hydrodeoxygenation of furfural to 2-methylfuran on molybdenum carbide catalysts, *Catal. Sci. Technol.* 4 (2014) 2340–2352.
- [72] N.K. Nag, Characterization of  $\text{Mo}/\text{Al}_2\text{O}_3$  catalysts by low-temperature oxygen chemisorption, *J. Catal.* 92 (1985) 432–437.
- [73] V.V.D.N. Prasad, K.-E. Jeong, H.-J. Chae, C.-U. Kim, S.-Y. Jeong, Oxidative desulfurization of 4,6-dimethyl dibenzothiophene and light cycle oil over supported molybdenum oxide catalysts, *Catal. Commun.* 9 (2008) 1966–1969.
- [74] K. Amakawa, S. Wrabetz, J. Krohnert, G. Tzolova-Muller, R. Schlogl, A. Trunschke, In situ generation of active sites in olefin metathesis, *J. Am. Chem. Soc.* 134 (2012) 11462–11473.
- [75] W.-S. Lee, A. Kumar, Z. Wang, A. Bhan, Chemical titration and transient kinetic studies of site requirements in  $\text{Mo}_2\text{C}$ -catalyzed vapor phase anisole hydrodeoxygenation, *ACS Catal.* 5 (2015) 4104–4114.
- [76] M.M. Sullivan, J.T. Held, A. Bhan, Structure and site evolution of molybdenum carbide catalysts upon exposure to oxygen, *J. Catal.* 326 (2015) 82–91.
- [77] W. Zhang, A. Desikan, S.T. Oyama, Effect of support in ethanol oxidation on molybdenum oxide, *J. Phys. Chem.* 99 (1995) 14468–14476.
- [78] M. Cherian, R. Gupta, M.S. Rao, G. Deo, Effect of modifiers on the reactivity of  $\text{Cr}_2\text{O}_3/\text{Al}_2\text{O}_3$  and  $\text{Cr}_2\text{O}_3/\text{TiO}_2$  catalysts for the oxidative dehydrogenation of propane, *Catal. Lett.* 86 (2003) 179–189.
- [79] S.T. Oyama, R. Radhakrishnan, M. Seman, J.N. Kondo, K. Domen, K. Asakura, Control of reactivity in C–H bond breaking reactions on oxide catalysts: methanol oxidation on supported molybdenum oxide, *J. Phys. Chem. B* 107 (2003) 1845–1852.
- [80] R. Kydd, W.Y. Teoh, J. Scott, D. Ferri, R. Amal, Probing surface properties and reaction intermediates during heterogeneous catalytic oxidation of acetaldehyde, *ChemCatChem* 1 (2009) 286–294.
- [81] Y. Azizi, C. Petit, V. Pitchon, Role of support in the oxidation of acetylene over gold catalysts, *J. Catal.* 269 (2010) 26–32.
- [82] S. Bedrane, C. Descorme, D. Duprez, Investigation of the oxygen storage process on ceria- and ceria–zirconia-supported catalysts, *Catal. Today* 75 (2002) 401–405.
- [83] X. Liu, K. Zhou, L. Wang, B. Wang, Y. Li, Oxygen vacancy clusters promoting reducibility and activity of ceria nanorods, *J. Am. Chem. Soc.* 131 (2009) 3140–3141.
- [84] X. Deng, S.Y. Quek, M.M. Biener, J. Biener, D.H. Kang, R. Schalek, E. Kaxiras, C.M. Friend, Selective thermal reduction of single-layer  $\text{MoO}_3$  nanostructures on Au (111), *Surf. Sci.* 602 (2008) 1166–1174.
- [85] E. Heracleous, M. Machli, A.A. Lemonidou, L.A. Vasalos, Oxidative dehydrogenation of ethane and propane over vanadia and molybdena supported catalysts, *J. Mol. Catal. A: Chem.* 232 (2005) 29–39.
- [86] H.J. Tian, E.L. Ross, I.E. Wachs, Quantitative determination of the speciation of surface vanadium oxides and their catalytic activity, *J. Phys. Chem. B* 110 (2006) 9593–9600.
- [87] L.J. Burcham, L.E. Briand, I.E. Wachs, Quantification of active sites for the determination of methanol oxidation turn-over frequencies using methanol chemisorption and in situ infrared techniques. 1. Supported metal oxide catalysts, *Langmuir* 17 (2001) 6164–6174.
- [88] L.J. Burcham, I.E. Wachs, The origin of the support effect in supported metal oxide catalysts: in situ infrared and kinetic studies during methanol oxidation, *Catal. Today* 49 (1999) 467–484.
- [89] L.J. Burcham, M. Badlani, I.E. Wachs, The origin of the ligand effect in metal oxide catalysts: novel fixed-bed in situ infrared and kinetic studies during methanol oxidation, *J. Catal.* 203 (2001) 104–121.
- [90] I.E. Wachs, Y. Chen, J.M. Jehng, L.E. Briand, T. Tanaka, Molecular structure and reactivity of the Group V metal oxides, *Catal. Today* 78 (2003) 13–24.
- [91] M.V. Ganduglia-Pirovano, C. Popa, J. Sauer, H. Abbott, A. Uhl, M. Baron, D. Stacchiola, O. Bondarchuk, S. Shaikhtudinov, H.J. Freund, Role of ceria in oxidative dehydrogenation on supported vanadia catalysts, *J. Am. Chem. Soc.* 132 (2010) 2345–2349.
- [92] R.S. Weber, Molecular-orbital study of C–H bond breaking during the oxidative dehydrogenation of methanol catalyzed by metal-oxide surfaces, *J. Phys. Chem.* 98 (1994) 2999–3005.
- [93] A. Marafi, A. Stainslaus, A. Hauser, K. Matsushita, An investigation of the deactivation behavior of industrial  $\text{Mo}/\text{Al}_2\text{O}_3$  and  $\text{Ni-Mo}/\text{Al}_2\text{O}_3$  catalysts in hydrotreating Kuwait atmospheric residue, *Petrol. Sci. Technol.* 23 (2005) 385–408.
- [94] J. Datka, A. Turek, J. Jehng, I. Wachs, Acidic properties of supported niobium oxide catalysts: an infrared spectroscopy investigation, *J. Catal.* 135 (1992) 186–199.
- [95] M. Banares, I. Wachs, Molecular structures of supported metal oxide catalysts under different environments, *J. Raman Spectrosc.* 33 (2002) 359–380.
- [96] H. Hu, I.E. Wachs, Catalytic properties of supported molybdenum oxide catalysts: in situ Raman and methanol oxidation studies, *J. Phys. Chem.* 99 (1995) 10911–10922.